VKI Special Course on Physico-Chemical Models for High Enthalpy and Plasma Flows Modeling June 4-7, 2002

RADIATION AND NONEQUILIBRIUM COLLISIONAL-RADIATIVE MODELS

Christophe Laux
Mechanical Engineering Department
Stanford University
Stanford, CA 94305-3032

Contents

1. Introduction 4

2. Air radiation modeling 5

2.1. Electronic spectra of atoms 5

2.1.1. Quantum states 5

2.1.2. Electronic transitions in atoms 6

2.1.3. Line broadening 7

2.1.4. Spectral emission coefficient for atomic transitions 7

2.1.5. Spectral absorption coefficient for atomic transitions 8

2.1.6. Atomic databases 8

2.2. Electronic spectra of diatomic molecules 9

2.2.1. Electronic states 9

2.2.2. Electronic selection rules 10

2.2.3. Rovibronic term energies 12

2.3.5. Rotational selection rules 15

2.3.6. Example: Rovibronic term energies of the $A^3\Sigma_u^+$ and $B^3\Pi_g$ states of N_2 16

2.3.7. Spectral emission coefficient for molecular transitions 17

3. Experimental validation of the SPECAIR code 19

3.1. Introduction 19

3.2. Spectral measurements 21

3.2.1. Experimental set-up 21

3.2.2. Thermodynamic state of the plasma 22

3.2.3. Spectral measurements 24

3.3. SPECAIR model of the plasma torch emission spectrum 25

3.4. Comparison SPECAIR-Experiments 26

3.4.1. Overview comparison 26

3.4.2. Range 185-280 nm 28

3.4.3. Range 280-500 nm 32

3.4.4. Range 500-800 nm *34*

3.4.5. Vacuum Ultraviolet *36*

4. Collisional-radiative modeling of nonequilibrium nitrogen plasmas 38

4.1. Introduction 38

4.2. Nitrogen CR model 39

4.2.1. Species and energy levels considered *39*

4.2.2. Reactions considered *39*

4.2.3 Example of rate coefficient calculation: N_2 ground state ionization by electron impact *41*

5. Application of the CR model to the analysis of a nonequilibrium recombining nitrogen plasma 42

5.1. Nonequilibrium factors 42

5.2. Recombining nitrogen plasma experiment 43

5.3. Analysis of the recombination experiments with the nitrogen CR model 45

6. Conclusions 50

7. Acknowledgments 50

8. References 51

1. Introduction

The radiative properties of air plasmas are of interest in a wide range of applications, including the design of thermal protection systems [1-3], detection of hypersonic missile signatures [4-6], astronomy [7], testing and validation of aerothermochemistry models [8], and optical diagnostics. Over the past four decades, space programs have stimulated intense research on air plasma radiation, both experimentally [9-23] and theoretically with the development of equilibrium [24-36] and nonequilibrium [37-40] radiation codes.

Air radiation modeling involves the determination of population distributions over internal quantum energy levels (rotational, vibrational, electronic), and of the radiative contribution of each of these levels. The radiation emitted by the plasma (bound-bound transitions) can be formally expressed as $\sum_{i,j} n_i R_{ij}$, where n_i represents the population of internal level i, and R_{ij} the radiation emitted by a transition from level i to any other level j. The summation extends over all internal energy levels i of atoms and molecules, and over all possible transitions from level i to j.

Under equilibrium conditions, the internal level populations n_i are determined using chemical equilibrium and Boltzmann distribution relations that only require knowledge of the temperature and pressure. Thus the radiative part (i.e. the R_{ij} coefficients) of radiation models can be tested and validated through comparisons with measurements obtained in equilibrium plasmas.

Under nonequilibrium conditions, the internal level populations are obtained by solving a system of rate equations involving all possible reactions between the internal levels of atoms and molecules. This system of equations, often called the Master Equation, is solved by a Collisional-Radiative (CR) or Excitation model.

This lecture addresses the topics of radiation and collisional-radiative modeling. For each topic, we begin by giving an overview of appropriate models, then we illustrate the use of the models for the interpretation of specific experiments. Accordingly, the lecture is divided into four sections. Section 2 reviews the approach used in the air plasma radiation model (SPECAIR) developed at Stanford on the basis of the NASA code NEQAIR. In Section 3, we discuss experimental validations of SPECAIR through comparisons with the measured absolute emission spectrum of an equilibrium air plasma. Section 4 describes a collisional-radiative (CR) model that we developed for molecular nitrogen plasmas. Finally in Section 5 we illustrate how the CR model can be applied to analyze the nonequilibrium radiation emitted by a recombining nitrogen plasma.

2. Air radiation modeling

2.1. Electronic spectra of atoms

2.1.1. Quantum states

The energy states of an atom are obtained from the time-independent Schrödinger equation:

$$\hat{H}\Psi = E\Psi$$

where $\hat{H}$ represents the Hamiltonian operator, E the total (kinetic + potential) energy of the atom, and ψ the wavefunction of the given state. The square modulus $|\psi|^2$ of the wavefunction corresponds to the probability density of finding the atom in the given state. The Schrödinger equation admits only discrete solutions (eigenvalues) which are the quantized energy states.

Individual electrons are characterized by five quantum numbers:

- n principal quantum number: 1,2,…
- l orbital quantum number: 0,1,…,n-1 (noted s, p, d, f,…)
- m_l orbital magnetic quantum number: 0, ±1, …, ±l (2l+1 values)
- s spin quantum number: ½
- m_s magnetic spin quantum number: ½, -½

A wavefunction for a one-electron system system is called an *orbital*. The set of orbitals having the same principal quantum number n is referred to as a *shell*, and the set of orbitals with the same n and l is called a *subshell*. The subshells are referred to as 1s, 2s, 2p, 3s, 3p,… According to the Pauli exclusion principle, a subshell nl may contain at most 2(2l+1) electrons. The number of electrons in each subshell is indicated with a superscript to the subshell designation. According to the *building-up* principle, the ground state configuration of atomic nitrogen (which has a total of 7 electrons) can be written as:

$$\text{N: } 1s^2\ 2s^2\ 2p^3$$

If one of the *2p* electrons is excited to a higher subshell, for instance 3s, the configuration of the excited electronic level is $1s^2\ 2s^2\ 2p^2\ 3s$.

For the majority of electronic transitions in common atoms, the orbital angular momenta of individual electrons are strongly coupled to one another, and similarly, the spins of individual electrons are also strongly coupled. The resultant angular momentum J is formed by vector addition of the resultant (i.e. summed over all electrons) spin, denoted by S, and the resultant orbital angular momentum denoted by L. This situation is called LS coupling. L takes the values 0, 1, 2, 3… and is denoted by the capital letters S, P, D, F,… For each configuration, there exist several possible energy levels called the *terms*. Each term, written as ^{2S+1}L, comprises a multiplet of electronic levels, each with a total angular momentum quantum number J = L+S,…|L-S|. The multiplet terms are written as $^{2S+1}L_J$. The degeneracy of each $^{2S+1}L_J$ level is equal to 2J+1, which corresponds to the 2J+1 Zeeman states (degenerate in the absence of a magnetic field). As an example, Figure 1 shows the terms of atomic nitrogen in the $1s^2\ 2s^2\ 2p^2$ 3s configuration.

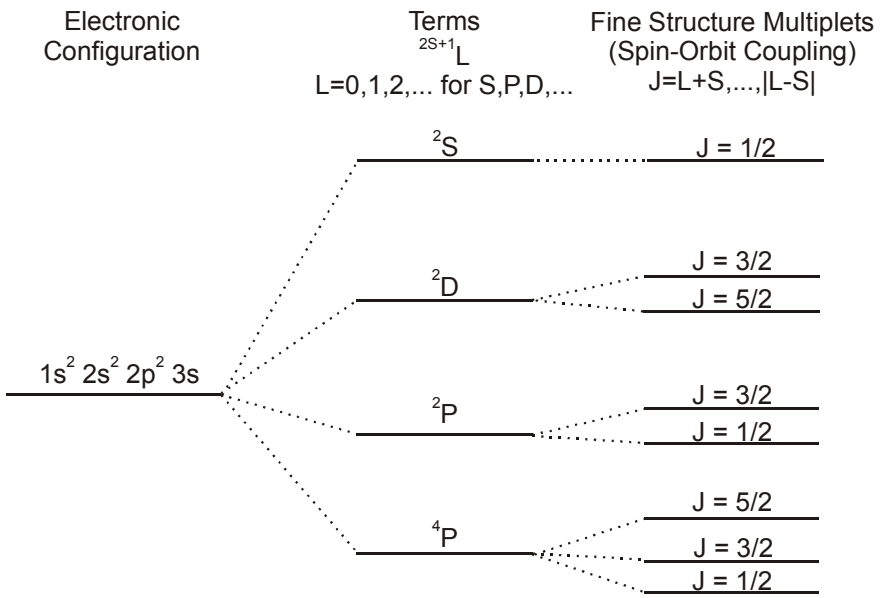


Figure 1. Electronic energy levels of atomic nitrogen in the $1s^2\ 2s^2\ 2p^2\ 3s$ configuration

2.1.2. Electronic transitions in atoms

We now consider the possible transitions between two electronic levels written as n'l' $^{2S'+1}L'_{J'}$ and n"l" $^{2S"+1}L"_{J"}$. (It is usual to designate upper levels with a prime, and lower levels with a double prime). Note that we consider only electric dipole transitions here (electric quadrupole, magnetic dipole, and magnetic quadrupole transitions are much weaker and generally not observed in emission). Selection rules issued from quantum mechanical considerations stipulate which transitions are allowed (as opposed to "forbidden" transitions that are weak). These rules are:

- Δn anything
- Δl ± 1
- Parity must change (terms of odd parity are indicated by superscript ^{o}, e.g. $^4S^o$ in Figure 2)

In the case of LS coupling, we have the additional rules:

- ΔS 0
- ΔL $0,\pm 1$ (except $L = 0 \leftrightarrow L = 0$)
- ΔJ $0,\pm 1$ (except $J = 0 \leftrightarrow J = 0$)

As an illustration, Figure 2 shows the allowed transitions between the (3p $^4S^o$) and (3s ^4P) terms of atomic nitrogen.

The difference of energy between levels can be expressed in various forms.

$$\Delta E = h\nu = hc\bar{\nu} = hc/\lambda = hc_{air}/\lambda_{air}\ ,$$

where h is Planck's constant (6.63×10^{-34} J.s), c is the speed of light in vacuum (nominally 3.0×10^8 m/s), λ is the wavelength of the radiation. Spectroscopists traditionally express the

energy difference with $\bar{\nu}$ in cm^{-1} ($\bar{\nu}$ is called the wavenumber). If the wavelength is measured in air, the wavelength must be corrected for the index of refraction of air at that wavelength. In the UV-Visible range, the correction is of the order of 0.1 nm.

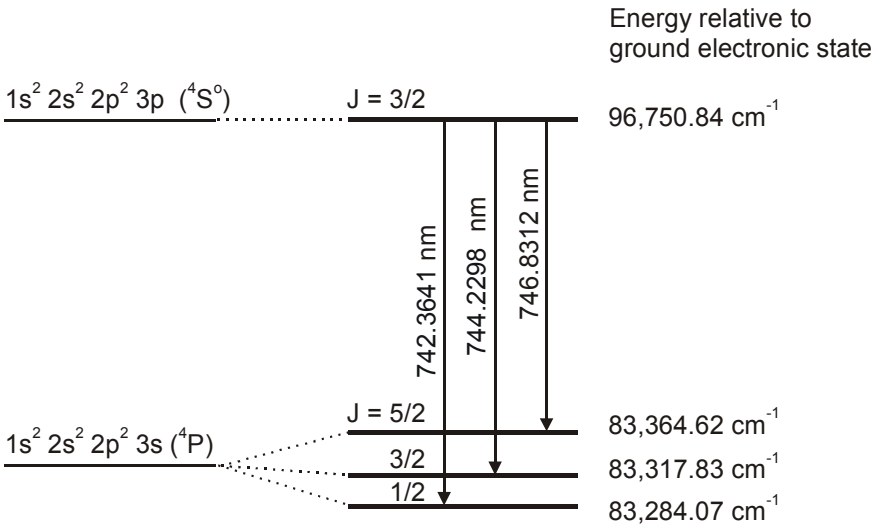


Figure 2. Allowed electronic transitions between the 3p $^4S^o$ and 3s ^4P terms of N. (Note that we indicate the wavelengths in air).

2.1.3. Line broadening

Atomic transitions do not appear as Dirac lines in the spectrum, but rather are spread over a narrow range of frequencies defined by the lineshape function, $\Phi(\nu-\nu_0)$, where ν_0 designates the line center. The lineshape is determined by a combination of line broadening mechanisms that include Doppler, natural, pressure, and Stark broadening. For molecular transitions, another possible mechanism of broadening is predissociation broadening. Doppler broadening leads to a Gaussian profile, and the other three mechanisms lead to a Lorentzian profile. The combination of the Gaussian and Lorentzian profile is a Voigt profile. A full discussion of the lineshape broadening is beyond the scope of this lecture, but interest readers can find more details in a number of sources, including Ref. [41].

2.1.4. Spectral emission coefficient for atomic transitions

The spectral emission coefficient due to a transition between upper electronic level u to lower electronic level l is:

$$\varepsilon(\nu) = n_u \frac{A_{ul}}{4\pi} \left(E_u - E_l\right)\Phi(\nu - \nu_0) \tag{1}$$

where n_u is the population of the upper level, A_{ul} is the Einstein A coefficient for spontaneous emission, E_u and E_l are the energies of the upper and lower levels respectively, and $\Phi(\nu-\nu_0)$ is

the lineshape function. Note that $E_u - E_l = h\nu_0$. The spectral emission coefficient is often expressed in units of [$W.cm^{-3}.sr^{-1}.\mu m^{-1}$].

For electric dipole transitions, the Einstein coefficient itself can be expressed as [42]:

$$A_{ul} = \frac{64\pi^4 \nu^3}{3\varepsilon_0 hc^3} \mu_{ul}^2$$

where ε_0 is the permittivity of free space and μ_{ul} is the transition dipole moment. It is clear from this equation that Einstein A coefficients tend to be largest at short wavelengths.

The population n_u of the upper state can be either obtained from collisional-radiative calculations, or calculated from the following relation if the electronic levels follow a Boltzmann distribution at temperature T:

$$n_u = \frac{g_u \exp(-E_u/kT)}{\sum_i g_i \exp(-E_i/kT)} n_A$$

where $g_u = 2J+1$ is the degeneracy of the electronic level, and n_A is the total population of the atom. The term in the denominator is called the electronic partition function and is usually denoted by Q_{el}. If the gas is in Local Thermodynamic Equilibrium, then the electronic levels follow a Boltzmann distribution at the gas temperature T_{gas}.

2.1.5. Spectral absorption coefficient for atomic transitions

The spectral absorption coefficient, typically expressed in units of [cm^{-1}], is related to the spectral emission coefficient as follows:

$$k(\nu) = \varepsilon(\nu) / B(\nu)$$

where B_ν is the Planck function defined as:

$$B(\nu) = \frac{2h\nu^3 / c^2}{\exp(h\nu/kT) - 1}$$

2.1.6. Atomic databases

The previous discussion was meant to introduce the reader to the various parameters that enter the calculation of the spectral emission coefficient. In practice, it is not necessary to calculate Einstein coefficients or energies, nor to determine the applicable selection rules, because extensive databases exist for the electronic transitions of atoms of common interest (see http://cfa-www.harvard.edu/amdata/ampdata/amdata.shtml for a list of available databases). For air species in particular (N, O, C), the interested reader is referred to the 1996 NIST ASD database published in Ref. [43] (online version: [44]).

2.2. Electronic spectra of diatomic molecules

2.2.1. Electronic states

We now turn our attention to the modeling of molecular spectra, and more specifically the modeling of transitions between electronic levels of diatomic molecules. The notations parallel those for atoms, as illustrated in the potential energy diagram of N_2 shown in Figure 3. We will begin by reviewing the definitions of electronic terms.

As can be seen from Figure 3, term energy levels are denoted by $X^1\Sigma_u^+$, $A^3\Sigma_u^+$, $B^3\Pi_g$,…The general notation is:

$$^{2S+1}\Lambda$$

where S is the quantum number associated with the total electron spin, and Λ is the quantum number associated with the absolute value of the projection of the orbital angular momentum along the internuclear axis. The quantity 2S+1 is called the spin multiplicity. The notation is preceded by a letter, which is generally X for the ground state, the sequence of letters A,B,C,…for states of a given multiplicity, and a,b,c,…for states of another multiplicity. Λ can take the values 0,1,2,3… associated with the Greek letters Σ, Π, Δ, Φ,…

Each electronic state $^{2S+1}\Lambda$ is split into 2*S*+1 spin substates (spin-splitting), and if Λ≥1 (i.e. for all states except Σ states) each spin substate is further split into two Λ–substates (Λ-doubling). Thus the degeneracy of electronic level $^{2S+1}\Lambda$ is given by

$$g_{el} = (2S+1)\,(2-\delta_{0,\Lambda})$$

where $\delta_{0,\Lambda}$ is the usual Kronecker delta. In summary, the electronic degeneracy is 2*S*+1 for Σ states, and 2(2*S*+1) for all other states.

Examples of Electronic State Notation

$^1\Sigma$	singlet sigma state	S=0, Λ =0, electronic degeneracy *g* = 1
$^2\Pi$	doublet pi	S=1/2, Λ =1, *g* = 4
$^3\Sigma$	triplet sigma	S=1, Λ =0, *g* =3
$^3\Pi$	triplet pi	S=1, Λ =1, *g* =6
$^2\Delta$	doublet delta	S=1/2, Λ =2, *g* =4

For molecules with nuclei of equal charges, a subscript (*g* or *u*) is placed to the right of the term symbol $^{2S+1}\Lambda$. This symbol indicates the symmetry of the electronic wavefunction with respect to the symmetry operator î, which inverts the coordinates of the nuclei and electrons relative to the center of mass of the molecule. If the electronic wavefunction does not change sign with î, the state is noted *g* (*gerade*), and otherwise *u* (*ungerade*).

For Σ states, a superscript (+ or –) is added to the right of the term symbol $^{2S+1}\Lambda$. This sign indicates the symmetry of the electronic wavefunction relative to the symmetry operator σ_v,

which corresponds to a mirror reflection through a plane containing the internuclear axis. If the wavefunction does not change sign, the state is denoted Σ^+, and otherwise Σ^-.

For non-sigma states, one may also encounter subscript (*r* or *i*) to the right of the term symbol. This symbol does not indicate a parity property of the wavefunction, but rather whether the state is regular (*r*) or inverted (*i*). We will discuss this later.

Finally, it is common to find the notation $^{2S+1}\Lambda_\Omega$ to designate the spin substates. The subscript Ω is the quantum number associated with the projection of the total angular momentum **J** along the internuclear axis. Note that this notation parallels the designation $^{2S+1}L_J$ for atomic levels. For a diatomic molecule, the total angular momentum exclusive of nuclear spin is the vector sum of orbital (**L**), spin (**S**), and rotational (**R**) angular momenta**, J** = **L** + **S** + **R**. The projection of **R** along the internuclear axis is of course zero, the projection of **L** is $\Lambda\hbar$ units of angular momentum, the projection of **S** is $\Sigma\hbar$, and the projection of **J** is $\Omega\hbar$. For a $^2\Pi$ state ($\Lambda=\pm1,\Sigma=\pm1/2$), Ω takes the values 3/2, 1/2, -1/2, and –3/2. It is customary to simply denote the spin substates with $|\Omega|$ and to distinguish the substates corresponding to positive or negative Ω by their parity. For parity designation, we use the (e,f) labeling scheme recommended by Brown et al [45]. Thus the four $^2\Pi$ substates are labeled $^2\Pi_{3/2,e}$, $^2\Pi_{3/2,f}$, $^2\Pi_{1/2,e}$ and $^2\Pi_{1/2,f}$. For a $^3\Pi$ state ($\Lambda=\pm1,\Sigma=1,0,-1$), we have $^3\Pi_{2,e}$, $^3\Pi_{2,f}$, $^3\Pi_{1,e}$, $^3\Pi_{1,f}$, $^3\Pi_{0,e}$, and $^3\Pi_{0,f}$. For a $^3\Sigma$ state ($\Lambda=0$, $\Sigma=1,0,-1$), we have $^3\Sigma_{1,e}$, $^3\Sigma_{1,f}$, and either $^3\Sigma_{0,e}$ or $^3\Sigma_{0,f}$. This notation poses a problem when $S>|\Lambda|>0$. In this case, the labeling is based on the value of $\Omega=|\Lambda| + \Sigma$. As an example, the eight substates of a $^4\Pi$ state are $^4\Pi_{5/2,e}$, $^4\Pi_{5/2,f}$, $^4\Pi_{3/2,e}$, $^4\Pi_{3/2,f}$, $^4\Pi_{1/2,e}$, $^4\Pi_{1/2,f}$, $^4\Pi_{-1/2,e}$.and $^4\Pi_{-1/2,f}$.

2.2.2. Electronic selection rules

Electric dipole allowed transitions between term electronic levels obey the following selection rules:

- $\Delta S \quad 0$
- $\Delta\Lambda \quad 0,\pm1$
- $u \leftrightarrow g$
- $\Sigma^+ \leftrightarrow \Sigma^+$ or $\Sigma^- \leftrightarrow \Sigma^-$

Figure 4 shows most known electronic transitions of the N_2 molecule. Each electronic transition is designated by a name that can be the name of the first researcher(s) to observe the transition (e.g.: the Worley-Jenkins transition which corresponds to the $c_3{}^1\Pi_u$-$X^1\Sigma_g^+$ transition of N_2), a Greek letter (e.g. γ for the $A^2\Sigma^+$-$X^2\Pi_r$ transition of NO), or the location where the transition appears in the positive column of a glow discharge (e.g. First Positive System for the $B^3\Pi_g$-$A^3\Sigma_u^+$ transition of N_2). Note that the transitions from excited triplet states to the ground state are spin forbidden. The difference of energy between two electronic levels gives an approximate idea of the frequency or wavelength region where the spectra will be observed.

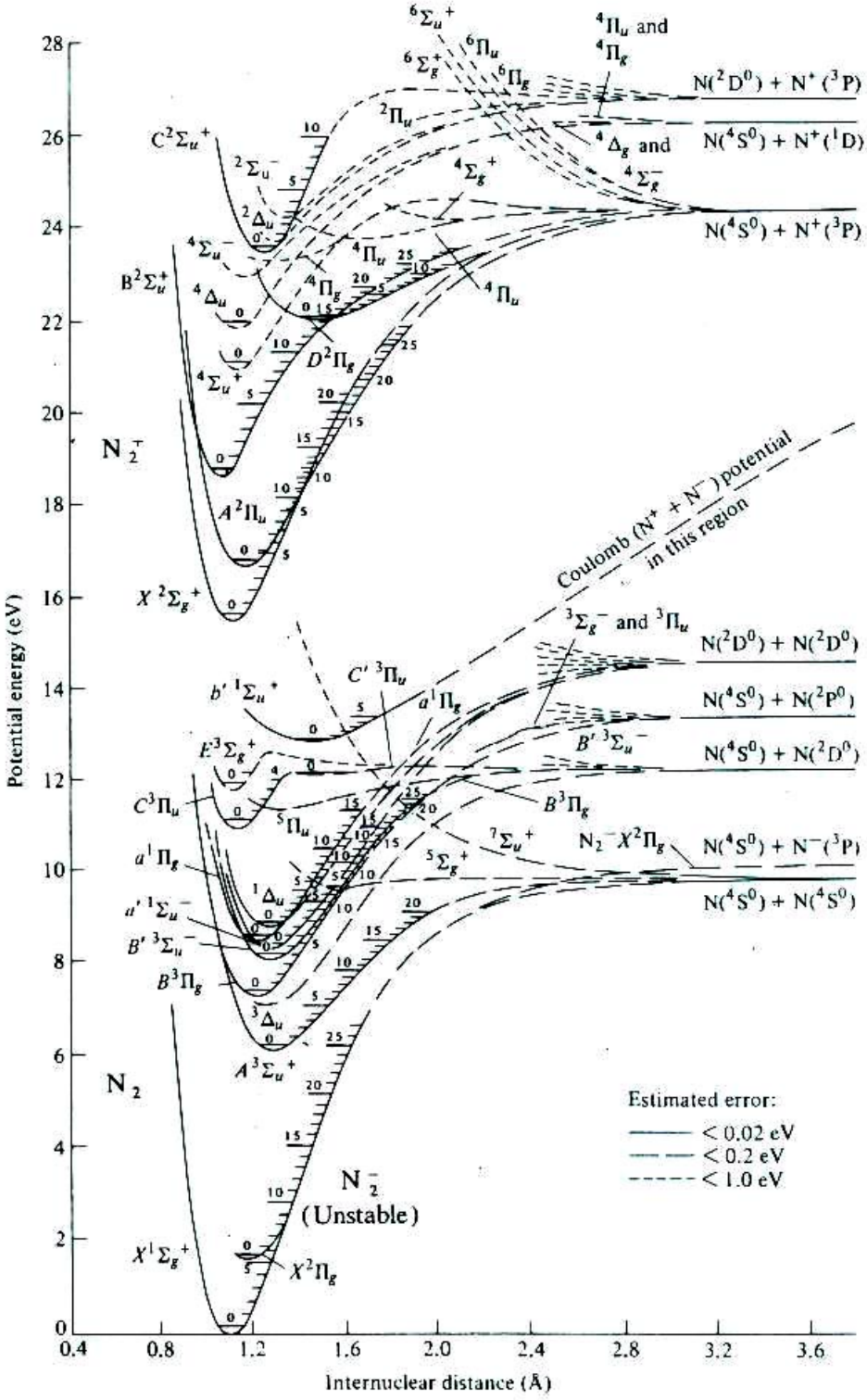


Figure 3. Potential energy diagram for N_2 compiled by F.R. Gilmore [46]

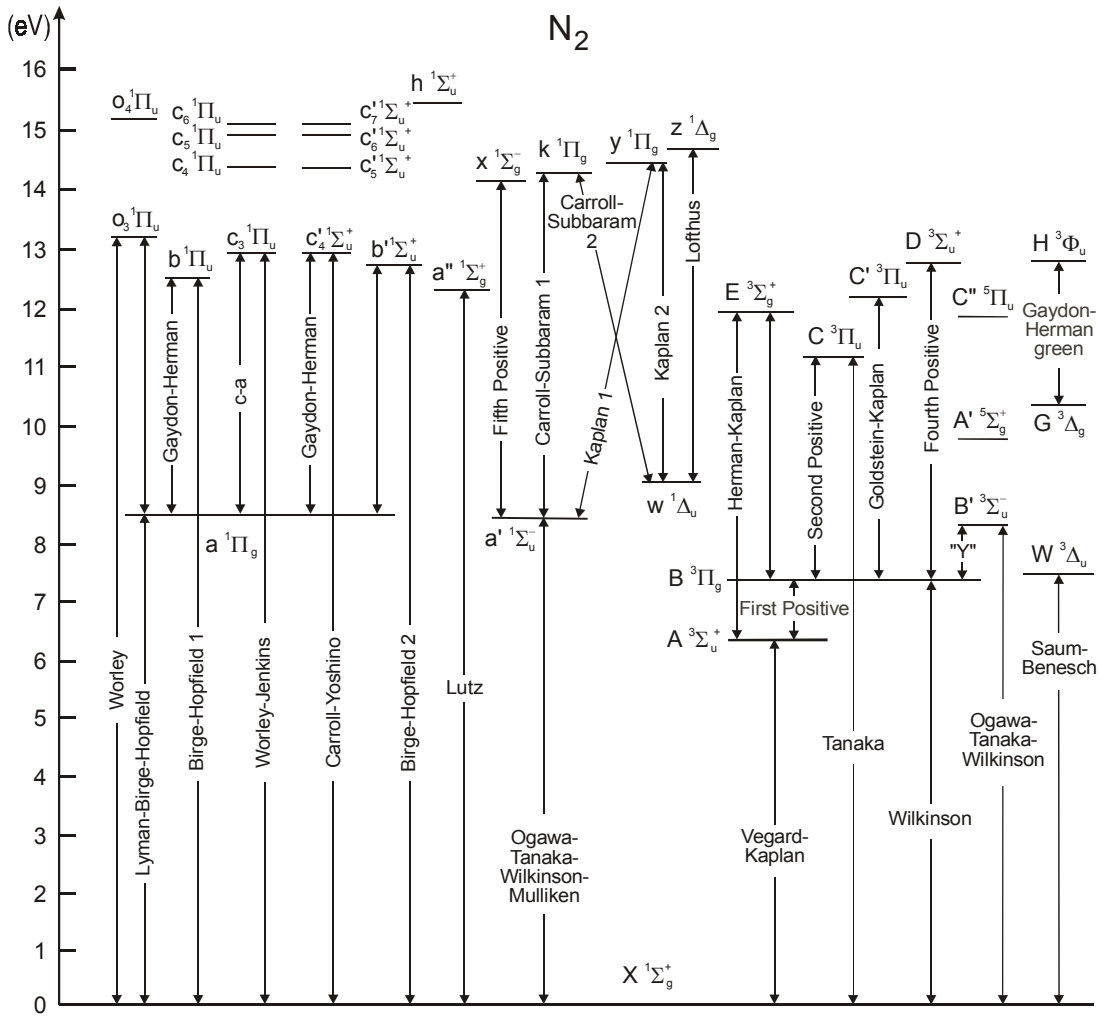


Figure 4. Simplified electronic energy level diagram for N_2 with observed transitions (note that certain transitions such as the Vegard-Kaplan is not electric dipole allowed and therefore appears only as a very weak transition)

2.2.3. Rovibronic term energies

Molecular electronic levels are divided into vibrational and rotational levels, and transitions will occur between pairs of these levels. The internal energy of a molecule in a given rovibronic level (e,v,J), where the three terms represent the electronic, vibrational, and rotational level, is given by:

$$T_{evJ} = \underbrace{T_e}_{\text{electronic}} + \underbrace{G(v)}_{\text{vibrational}} + \underbrace{F(J)}_{\text{rotational}}$$

For diatomic molecules such as N_2, O_2, NO, or N_2^+, the typical energy spacing between adjacent vibrational levels is of the order of 2000 cm^{-1}, and the typical energy spacing between adjacent rotational levels is about 2 cm^{-1}. The electronic and vibrational term energies are often grouped into a single term designated by T_v. For a general detailed discussion of rotational

energy levels, the reader is referred to Herzberg [47], Bernath [48], Steinfeld [49], and [50]. We summarize below the various notations used for rotational term substates.

For rotational levels, the (2S+1) spin substates are labeled F_1, F_2, …F_{2S+1} and they are further defined by their parity. The parity is an important parameter because it represents the symmetry of the wavefunctions and therefore the selection rules for transitions between rovibronic levels. As already mentioned, the (e,f) labeling scheme proposed by Brown *et al.* [45] is employed because it is particularly convenient for selection rules. With these definitions, F(J) is denoted by:

For $\Lambda=0$ (Σ states): $F_{1,e\text{ or }f}$, $F_{2,e\text{ or }f}$,… $F_{2S+1,e\text{ or }f}$ (total of 2S+1 states)
For $\Lambda\neq0$ (Π, Δ, Φ,...): $F_{1,e}$, $F_{1,f}$, $F_{2,e}$, $F_{2,f}$,… $F_{2S+1,e}$, $F_{2S+1,f}$ (total of 2(2S+1) states)

Furthermore, we also associate with each rotational level the quantum number N, which is the rotational quantum number exclusive of spin. Although N is only a good quantum number for Hund's case (b) coupling, there is always a one-to-one correspondence between the rotational levels in Hund's case (b) and any other coupling case, so that a value of N can always be assigned. When $J \geq \Lambda + S$, the spin substates F_i are associated with the following values of N:

$$\begin{cases} F_1: & J = N + S \\ F_2: & J = N + S - 1 \\ \vdots & \\ F_{2S+1}: & J = N - S \end{cases}$$

For a given value of J (not N!), the F_i substates are always ordered in increasing energy, such that $F_1(J) < F_2(J) < \ldots < F_{2S+1}(J)$.

If the parity (e,f) is not given, it can be determined using the following rules:

- If $[(-1)^J \times$ total parity of the rotational level$] > 0$: parity is e
- If $[(-1)^J \times$ total parity of the rotational level$] < 0$: parity is f
- If J is half integer, substitute (J-0.5) in the above expressions.

The total parity (+,-) of the rotational levels can be conveniently inferred from the diagrams introduced by Herzberg [47], pp. 238-239.

To illustrate, we consider the example of the $A^3\Sigma_u^+$ level of N_2. The energy diagram shown in Figure 5 is constructed from the diagrams of Herzberg ([47] p. 238). To first order, the energy spacing is determined by N. The substates are ordered as $F_1(J) < F_2(J) < F_3(J)$. Note however that we do not have necessarily $F_1(N) < F_2(N) < F_3(N)$: in fact, for the $A^3\Sigma_u^+$ level of N_2 we have $F_2(N) < F_1(N) < F_3(N)$.

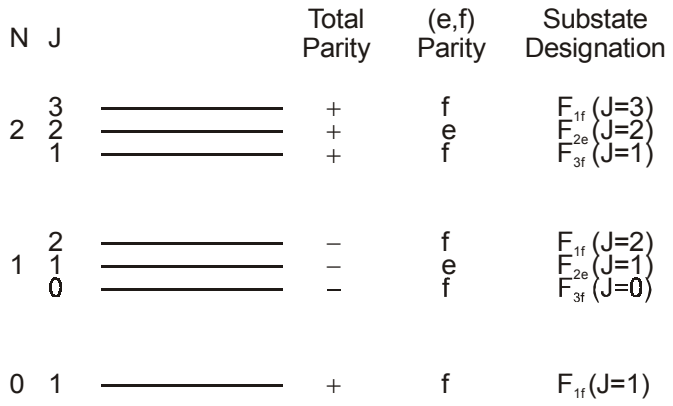


Figure 5. Rotational energy levels of the $A^3\Sigma_u^+$ level of N_2 (and more generally of any $^3\Sigma^+$ level).

It remains to relate the substates F_i to the term symbols ${}^{2S+1}\Lambda_\Omega$ for nonsigma substates ($\Lambda \geq 1$). (For sigma states, the association is not made.) For nonsigma substates, the assignment depends on whether the state is regular (*r*) or inverted (*i*). The designation depends on the sign of the spin-orbit coupling constant traditionally noted A. If A > 0, the smallest value of Ω is associated with the lowest energy level (i.e. F_1). In inverted states, the smallest value of Ω is associated with F_{2S+1}.

Consider as an example the $B^3\Pi_g$ level of N_2, which is a regular Π state because the spin-orbit constant A is about +42 cm^{-1}. Using again the energy diagrams of Herzberg ([47] p. 239), we obtain the diagram shown in Figure 6.

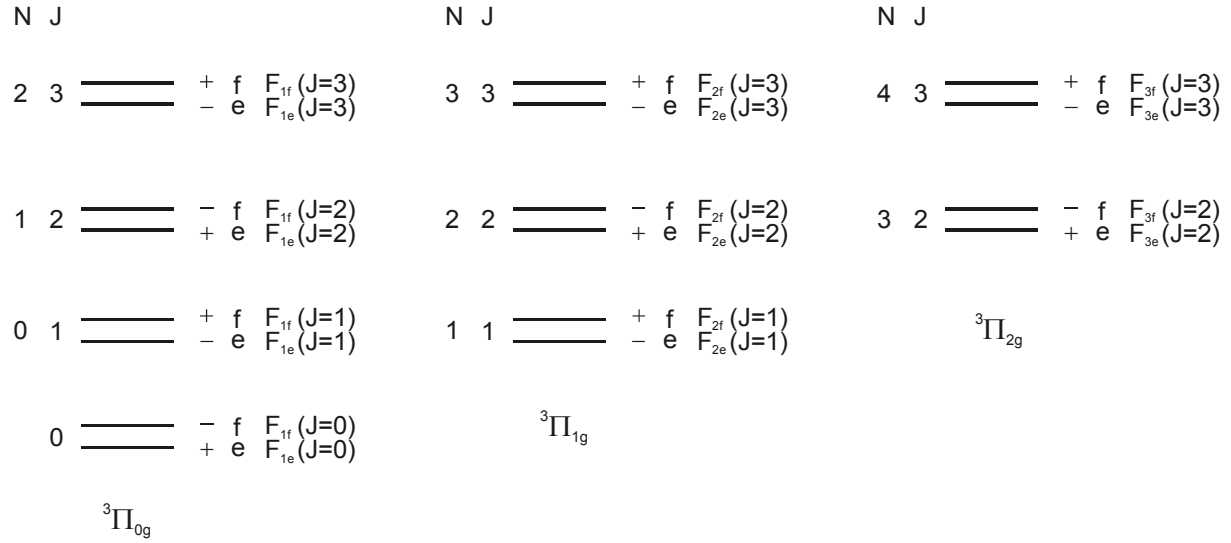


Figure 6. Rotational energy levels of the $B^3\Pi_g$ level of N_2 (and more generally of any regular $^3\Pi$ level).

2.3.5. Rotational selection rules

With the definitions of the previous section, the selection rules that determine electric dipole allowed transitions between pairs of rotational levels belonging to different vibronic levels are:

- $\Delta J \quad 0 \quad$ and $\quad e \leftrightarrow f$ (except $J = 0 \leftrightarrow J = 0$)
- $\Delta J \quad \pm 1 \quad$ and $\quad e \leftrightarrow e$ or $f \leftrightarrow f$

A group of lines with $\Delta J = -1$ forms a P branch, $\Delta J = 0$ forms a Q branch, and $\Delta J = 1$ forms an R branch. Similarly, letters are also associated with the various values of ΔN (see Table 1).

Table 1. Letter designations for changes in N and J in a transition

ΔJ				–1	0	1			
ΔN	...	–3	–2	–1	0	1	2	3	...
Designation		N	O	P	Q	R	S	T	

The various branches corresponding to different changes in J and N occurring during the transition are based on the letter designations of Table 1, on the F_i assignment of the upper and lower substate, and on either J', J", N', or N". A typical notation is:

$$^{\Delta N}\Delta J_{i'i"}(J')$$

If $\Delta N = \Delta J$, then the upper letter is not included and if $F_i' = F_i"$, then only one subscript is included (e.g., $^{P}P_{11}$ is simply noted P_1). An example of transition labeling is given in Figure 7.

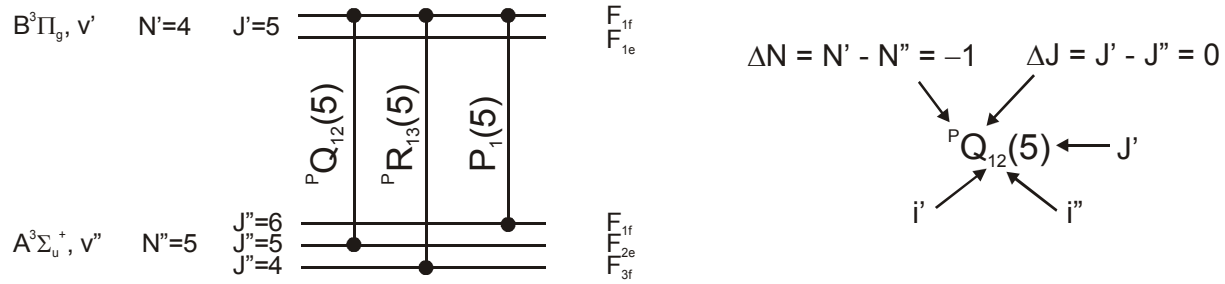


Figure 7. Allowed transitions between two sets of rovibronic levels belonging to the N_2 B and A states. There is a total of 27 branches for $^3\Pi$-$^3\Sigma$ transitions.

The energy change during a transition is usually more closely associated with ΔN than with ΔJ. Therefore, the form of the branch is also primarily controlled by ΔN. Hence, the $^{P}Q_{12}$ branch is called the P form Q branch. For transitions with $\Delta\Lambda = 0$ (e.g. $\Sigma - \Sigma$, $\Pi - \Pi$ transitions), the P and R branches are intense, and the Q branch is weak. For $\Delta\Lambda = \pm 1$, the P,Q, and R branches have comparable intensities. The strength of each branch is determined by the rotational line strength factor discussed in Section 2.3.7.

2.3.6. Example: Rovibronic term energies of the $A^3\Sigma_u^+$ and $B^3\Pi_g$ states of N_2

The N_2 $B^3\Pi_g$-$A^3\Sigma_u^+$ transition, also called the first positive system of N_2, has been the subject of extensive spectroscopic investigations using Fourier-transform spectrometry, in particular by Roux *et al*. [51, 52] who determined molecular parameters for the array of vibrational levels $0 \le v_A \le 16$ of the $A^3\Sigma_u^+$ state and $0 \le v_B \le 21$ of the $B^3\Pi_g$ state by fitting wavenumbers calculated by diagonalizing upper and lower state Hamiltonian matrices to experimental wavenumbers. The SPECAIR model is based on these results. Rotational term energies and line positions for the B and A states of N_2 are determined by diagonalization of the $^3\Pi$ and $^3\Sigma^+$ Hamiltonians given in Ref. [51], respectively. Effective term energies and molecular parameters for levels $0 \le v_A \le 16$ and $0 \le v_B \le 21$ are taken from Refs. [51] and [52]. The matrix elements have the following expressions:

Matrix elements of the $^3\Sigma^+$ Hamiltonian in a parity case (a) basis set for N_2 (Table 2, Ref. [51])

$$\left\langle {}^3\Sigma_0^+ \middle| H \middle| {}^3\Sigma_0^+ \right\rangle = \frac{1}{2}(1\mp1)\left[T_{\Sigma eff} - 2\varepsilon^*_{\Sigma eff} \pm \alpha^*_{\Sigma eff} + B_{\Sigma eff}(x+2) - 2\gamma^*_{\Sigma eff} - D_\Sigma\left(x^2+8x+4\right) + H_\Sigma\left(x^3+18x^2+28x+8\right)\right]$$

$$\left\langle {}^3\Sigma_1^+ \middle| H \middle| {}^3\Sigma_1^+ \right\rangle = T_{\Sigma eff} + \varepsilon^*_{\Sigma eff} + B_{\Sigma eff}\,x - \gamma^*_{\Sigma eff} - D_\Sigma\left(x^2+2x(1\mp1)\right) + H_\Sigma\left(x^3+2(1\mp1)(3x^2+2x)\right)$$

$$\left\langle {}^3\Sigma_0^+ \middle| H \middle| {}^3\Sigma_1^+ \right\rangle = -\frac{1}{2}(1\mp1)\sqrt{x}\left[2B_{\Sigma eff} - \gamma^*_{\Sigma eff} - 4D_\Sigma(x+1) + H_\Sigma\left(6x^2+20x+8\right)\right]$$

Notes:
1. Upper and lower signs refer to e and f levels respectively
2. $x=J(J+1)$.
3. Table 2 of Ref. [51]) has erroneous factors (1 ± 1) instead of the correct (1 ∓ 1) factors for the $<{}^3\Sigma_1^+ | H | {}^3\Sigma_1^+>$ matrix element (Private communication, F. Roux, 1997). The above table has the correct signs

Matrix elements of the $^3\Pi$ Hamiltonian in a parity case (a) basis set for N_2 (Table 1, Ref. [51])

$$\left\langle {}^3\Pi_0 \middle| H \middle| {}^3\Pi_0 \right\rangle = T_{\Pi eff} - A_{\Pi eff} + \varepsilon^*_{\Pi eff} \pm \alpha^*_{\Pi eff} + B_\Pi(x+1) + \frac{1}{4}q_\Pi x + \frac{1}{2}(1\pm1)\left(q_\Pi + p_\Pi\right) - A_{D\Pi}(x+1) - D_\Pi\left(x^2+4x+1\right) - H_\Pi\left(x^3+9x^2+9x+1\right)$$

$$\left\langle {}^3\Pi_1 \middle| H \middle| {}^3\Pi_1 \right\rangle = T_{\Pi eff} - 2\varepsilon^*_{\Pi eff} + B_\Pi(x+1) + \frac{1}{4}q_\Pi(1\pm1)x + \frac{1}{2}\left(q_\Pi + p_\Pi\right) - D_\Pi\left(x^2+6x-3\right) + H_\Pi\left(x^3+15x^2-5x+5\right)$$

$$\left\langle {}^3\Pi_2 \middle| H \middle| {}^3\Pi_2 \right\rangle = T_{\Pi eff} + A_{\Pi eff} + \varepsilon^*_{\Pi eff} + B_\Pi(x-3) + \frac{1}{4}q_\Pi(x-2) + A_{D\Pi}(x-3) - D_\Pi\left(x^2-4x+5\right) + H_\Pi\left(x^3-3x^2+5x-7\right)$$

$$\left\langle {}^3\Pi_0 \middle| H \middle| {}^3\Pi_1 \right\rangle = -\left[B_\Pi + \left(\tfrac{1}{4}\pm\tfrac{1}{2}\right)q_\Pi + \left(\tfrac{1}{8}\pm\tfrac{1}{4}\right)p_\Pi - \tfrac{1}{2}A_{D\Pi} - 2D_\Pi(x+1) - \tfrac{1}{2}\gamma_\Pi + H_\Pi\left(3x^2+10x-1\right)\right]\sqrt{2x}$$

$$\left\langle {}^3\Pi_0 \middle| H \middle| {}^3\Pi_2 \right\rangle = -\left[2D_\Pi \mp \tfrac{1}{4}q_\Pi - 2H_\Pi(3x-1)\right]\sqrt{x(x-2)}$$

$$\left\langle {}^3\Pi_1 \middle| H \middle| {}^3\Pi_2 \right\rangle = -\left[B_\Pi + \tfrac{1}{4}q_\Pi + \tfrac{1}{8}p_\Pi + \tfrac{1}{2}A_{D\Pi} - 2D_\Pi(x-1) - \tfrac{1}{2}\gamma_\Pi + H_\Pi\left(3x^2-2x+3\right)\right]\sqrt{2(x-2)}$$

Notes:
1. Upper and lower signs refer to e and f levels respectively
2. $x=J(J+1)$.

The energy of a given rovibronic level (e,v,J) is calculated by diagonalizing the upper and lower state Hamiltonians given by the following matrix expressions:

$A^3\Sigma_u^+$ State Hamiltonian	$B^3\Pi_g$ State Hamiltonian
$\begin{pmatrix} \langle {}^3\Sigma_0^+ \lvert H \rvert {}^3\Sigma_0^+ \rangle & \langle {}^3\Sigma_0^+ \lvert H \rvert {}^3\Sigma_1^+ \rangle \\ sym & \langle {}^3\Sigma_1^+ \lvert H \rvert {}^3\Sigma_1^+ \rangle \end{pmatrix}$	$\begin{pmatrix} \langle {}^3\Pi_0 \lvert H \rvert {}^3\Pi_0 \rangle & \langle {}^3\Pi_0 \lvert H \rvert {}^3\Pi_1 \rangle & \langle {}^3\Pi_0 \lvert H \rvert {}^3\Pi_2 \rangle \\ sym & \langle {}^3\Pi_1 \lvert H \rvert {}^3\Pi_1 \rangle & \langle {}^3\Pi_1 \lvert H \rvert {}^3\Pi_2 \rangle \\ sym & sym & \langle {}^3\Pi_2 \lvert H \rvert {}^3\Pi_2 \rangle \end{pmatrix}$

The matrices are diagonalized for each rotational level J and for each (e,f) parity case. For the $A^3\Sigma_u^+$ state, we obtain three term energies for each J. These values are assigned to the F_1, F_2, and F_3 substates by noting that F_1, F_2, and F_3 are always ordered by increasing energy for given J. From Figure 5, we know that F_2 is of parity *e*, and F_1 and F_3 are both of parity *f*. $F_{1f}(J)$ and $F_{3f}(J)$ correspond to the smallest and largest eigenvalues, respectively, of the Hamiltonian calculated for the case of *f* parity. For the case of *e* parity, the $\langle {}^3\Sigma_0^+ \lvert H \rvert {}^3\Sigma_0^+ \rangle_e$ matrix element is zero, and $F_{2e}(J)$ is simply equal to $\langle {}^3\Sigma_1^+ \lvert H \rvert {}^3\Sigma_1^+ \rangle_e$.

For a given J level of the $B^3\Pi_g$ state, the Hamiltonian matrix has three eigenvalues in the e parity case. These values are ordered by increasing energy and are then assigned to F_{1e}, F_{2e}, and F_{3e}. A similar treatment is applied to the eigenvalues obtained in the case of f parity.

2.3.7. Spectral emission coefficient for molecular transitions

The spectral emission coefficient due to a transition from upper rovibronic level (e',v',J') to lower rovibronic level (e",v",J") is expressed using an expression similar to Equation (1):

$$\varepsilon(\nu) = n_{e'v'J'} \frac{A_{e'v'J'-e"v"J"}}{4\pi} \left(T_{e'v'J'} - T_{e"v"J"}\right) \Phi(\nu - \nu_0) \tag{2}$$

where $n_{e'v'J'}$ is the population of the upper level, $A_{e'v'J'-e"v"J"}$ is the Einstein A coefficient for spontaneous emission, $T_{e'v'J'}$ and $T_{e"v"J"}$ are the energies of the upper and lower levels respectively ($T_{e'v'J'} - T_{e"v"J"} = h\nu_0 \cong h\nu$) and $\Phi(\nu-\nu_0)$ is the lineshape function.

The Einstein coefficient itself can be expressed as:

$$A_{e'v'J'-e"v"J"} = \frac{64\pi^4\nu^3}{3\varepsilon_0 hc^3} \left|\mu_{e'v'J'-e"v"J"}\right|^2$$

where ε_0 is the permittivity of free space and $\mu_{e'v'J'-e"v"J"}$ is the transition dipole moment. The Einstein A can be expressed as:

$$A_{e'v'J'-e"v"J"} = \frac{64\pi^4\nu^3}{3\varepsilon_0 hc^3 \left(2-\delta_{0,\Lambda'}\right)(2S+1)} \left|R_e^{v'v"}\right|^2 \quad \frac{S_{J'J"}}{2J'+1} \tag{3}$$

where $S_{J'J''}$ is the so-called rotational line strength and $\left|R_e^{v'v''}\right|^2 = \left|\langle v'|R_e|v''\rangle\right|^2$ is the square of the electronic-vibrational transition moment. In the foregoing expression $|v'\rangle$ and $|v''\rangle$ are the vibrational wavefunctions of the upper and lower state respectively, and $R_e = \langle e'|\mu_e|e''\rangle$ is the electronic transition moment, equal to the average of the electric dipole moment μ_e with respect to the upper and lower state electronic wavefunctions $|e'\rangle$ and $|e''\rangle$.

The squared electronic-vibrational transition moment $\left|R_e^{v'v''}\right|^2$ measures the intrinsic strength of a transition from the upper vibronic state (e',v') to lower vibronic state (e'',v''). It is usually calculated from *ab initio* values of the electronic transition moment $R_e(r)$, where r is the internuclear distance, and from vibrational wavefunctions obtained from RKR potentials (see for instance Ref. [53]). The squared electronic-vibrational transition moment is sometimes approximated as:

$$\left|R_e^{v'v''}\right|^2 \cong \left|R_e\left(\bar{r}_{v'v''}\right)\right|^2 \left|\langle v'|v''\rangle\right|^2$$

where $\bar{r}_{v'v''} = \langle v'|r|v''\rangle$ is called the *r-centroid*, and $q_{v'v''} = \left|\langle v'|v''\rangle\right|^2$ is the Franck-Condon factor. In this formulation, $|R_e|^2$ measures the intrinsic strength of the electronic transition, and the Franck-Condon factor determines how the intensity is distributed among the combinations of (v',v''), also called the vibrational bands.

The rotational line strength factor $S_{J'J''}$ determines how the intensity is apportioned to the possible J'' levels or branches. It is recommended to use the convention of Whiting ([50], p. 81) for the electronic transition moment, and accordingly to use line strength factors normalized as follows:

$$\sum_{J''} S_{J'J''}(J'') = \left(2 - \delta_{0,\Lambda'+\Lambda''}\right)(2S+1)(2J'+1),$$

where the spin multiplicity $(2S+1)$ is the same for the upper and lower electronic states since we consider only spin-allowed transitions here. For spin-allowed transitions, the rotational line strength is called the Hönl-London factor. Hönl-London factors can be found in tabulated form in the literature (e.g. Kovacs [54]) or can be calculated from the method described in Refs. [50, 55-58]). In SPECAIR, we use Hönl-London factors computed with the numerical code of Whiting [56].

Combining Equations (2) and (3), we obtain:

$$\varepsilon(\nu) = n_{e'v'J'} \frac{16\pi^3\nu^4}{3\varepsilon_0 c^3\left(2-\delta_{0,\Lambda'}\right)(2S+1)}\left|R_e^{v'v''}\right|^2 \quad \frac{S_{J'J''}}{2J'+1} \quad \Phi(\nu-\nu_0) \tag{4}$$

The population $n_{e'v'J'}$ of the upper state can either be obtained from collisional-radiative calculations, or calculated from the following relation if the internal levels follow Boltzmann distributions at T_{el}, T_{vib}, and T_{rot}:

$$n_{\mathrm{e'v'J'}} = n_{total} \frac{g_{e'}\left(2\mathrm{J'}+1\right)\exp\left[-\dfrac{T_{\mathrm{e'}}}{kT_{\mathrm{el}}}-\dfrac{G\left(\mathrm{v'}\right)}{kT_{\mathrm{vib}}}-\dfrac{F\left(\mathrm{J'}\right)}{kT_{\mathrm{rot}}}\right]}{\sigma\sum\limits_{\mathrm{e,v,J}} g_e\left(2\mathrm{J}+1\right)\exp\left[-\dfrac{T_{\mathrm{e}}}{kT_{\mathrm{el}}}-\dfrac{G\left(\mathrm{v}\right)}{kT_{\mathrm{vib}}}-\dfrac{F\left(\mathrm{J}\right)}{kT_{\mathrm{rot}}}\right]} L\left(J', P'_{ef}, P'_{gu}\right)$$

where σ is a factor equal to 2 for homonuclear molecules and 1 for heteronuclear molecules, $g_{e'} = (2-\delta_{0,\Lambda'})(2S+1)$ is the degeneracy of the electronic level, n_{total} is the total population of the molecule, and $L\left(J', P'_{ef}, P'_{gu}\right)$ is the line alternation factor due to nuclear spin. Line intensity alternation due to nuclear spin in homonuclear diatomic molecules has been treated in detail by several authors (see for instance Herzberg [47], Whiting et al. [40], Hornkohl [58]). The line alternation factor $L(J,P_{ef},P_{gu})$ is equal to 1 for heteronuclear diatomic molecules and to the values listed in Table 2 for homonuclear diatomic molecules. Table 2 expresses the line alternation factors in terms of the (e,f) parity doublet labeling scheme.

Table 2. Line intensity factors for homonuclear molecules. The quantities P_{ef}, P_{gu}, and J* are defined as follows: P_{ef} = 1 if the upper level of the transition is of *e* parity, –1 if it is of *f* parity. P_{gu} = 1 if the upper electronic state is gerade, –1 if ungerade. J* = J for J integer, J* = J–1/2 for J half integer, where J is the rotational quantum number. I is the nuclear spin (equal to 1 for ^{14}N, and 0 for ^{16}O and ^{12}C).

$P_{ef}\times P_{gu}\times(-1)^{J^*}$	Line Intensity Factor, $L(J,P_{ef},P_{gu})$	
	I integer	I half integer
1	$(I+1)/(2I+1)$	$I/(2I+1)$
−1	$I/(2I+1)$	$(I+1)/(2I+1)$

3. Experimental validation of the SPECAIR code

3.1. Introduction

Developed at NASA Ames Research Center over the past three decades, the NEQAIR code [38] combines a line-by-line radiation model [28, 29] and a collisional-radiative model to predict the nonequilibrium populations of excited bound electronic states of air species. Since the publication of the original version in 1985, the radiation module of NEQAIR has undergone major changes [40]. Both the NEQAIR96 version developed at NASA Ames [40] and the SPECAIR version of Stanford [30-35] feature accurate transition probabilities and spectral line positions as well as additional radiative transitions. These improved data are the result of significant advances in computational chemistry and Fourier-Transform spectroscopy techniques, which have provided a wealth of accurate spectroscopic and transition probability data for the main radiative transitions of high temperature air.

The current SPECAIR model incorporates the 33 electronic transitions listed in Table 3. In addition, it comprises 1484 lines of atomic nitrogen from 86.523 nm to 54.83 μm, 856 lines of

atomic oxygen from 69.753 nm to 16.71 μm, and 1291 lines of atomic carbon from 94.519 nm to 12.28 μm.

Table 3. Molecular transitions modeled in SPECAIR with their (very) approximate spectral location.

VUV 80–200 nm	UV 200–400 nm	Visible 400–800 nm	Near-IR 800–1.5 μm	IR 1.5–6 μm
N_2 b–X (Birge-Hopfield 1)	O_2 B–X (Schumann-Runge)	N_2 B–A (first positive)	N_2^+ A–X (Meinel)	NO X-X
N_2 b'–X (Birge-Hopfield 2)	N_2 C–B (second positive)	CN A–X (red)	NO C-A	CO X-X
N_2 c_4'–X (Carroll-Yoshino)	N_2^+ B–X (first negative)		NO D-A	OH X-X
N_2 c_3–X (Worley-Jenkins)	NO B–X (β)		NO F-C	
N_2 o_3–X (Worley)	NO A–X (γ)		NO E-C	
N_2 e'-X	NO C–X (δ)		NO E-D	
	NO D–X (ε)		NO H-C	
	NO B'–X (β')		NO H-D	
	NO E–X (γ')		NO H'-C	
	CN B–X (violet)		NO H'-D	
	OH (A-X)			
	NH (A-X)			

Unlike NEQAIR, SPECAIR does not incorporate a collisional-radiative model for excited electronic states. Instead, the populations of emitting vibronic levels (e',v') are either calculated outside the code, using the collisional-radiative model presented in Section 4 of this lecture, or are calculated assuming Boltzmann distributions at T_{el} and T_{vib}. The rotational populations are always assumed to follow a Boltzmann distribution at T_{rot}.

An important step in testing nonequilibrium radiation models is to validate their predictions for equilibrium plasmas. In equilibrium plasmas, all populations can be calculated with knowledge of the temperature and pressure using chemical equilibrium and Boltzmann distribution relations. High temperature equilibrium plasmas are perhaps most conveniently produced with microwave (mw), radio-frequency (rf), or direct-current (dc) plasma torches. One advantage of these devices over shock tubes is that they can operate at atmospheric pressure where the high collision frequency promotes fast equilibration (in the current free region outside of the discharge and for relatively slow flow rates). Another advantage is that they produce steady-state flows with sufficiently long test-times for thermodynamic characterization experiments and spectral measurements.

In our work to validate the SPECAIR code in the spectral range 185–800 nm, we produced LTE air plasmas with a 50 kW radio-frequency inductively coupled plasma torch operating at

atmospheric pressure. The existence of LTE conditions at the exit plane of the plasma torch is supported by emission spectroscopy measurements of electronic, vibrational, and rotational temperatures, and of electron number densities. The temperature profile at the nozzle exit was measured with an accuracy of about ± 80 K, i.e. ± 1%. The chemical composition and internal state population distributions are entirely determined from equilibrium relations based on this measured temperature profile. Line-of-sight emission spectra were measured, corrected for the relative spectral response of the detection system, and placed on absolute intensity scales by means of sources of spectral radiance traceable to NIST standards. In contrast to previous experiments that had been limited to either NO bands, or N_2 and N_2^+ bands, the broad spectral range (185-800 nm) and high temperature conditions (~7500 K) of the present work afford access to the emission of about a dozen electronic systems emitted from molecular species including NO, N_2, N_2^+, CN, and O_2 as well as atomic lines of oxygen, nitrogen, and carbon. The calibrated, absolute intensity emission spectra of these well characterized plasmas can therefore be used as benchmarks to validate air radiation codes, in particular to test the accuracy of transition probability and spectroscopic databases, to determine whether enough radiative systems are considered, and to test the convergence of nonequilibrium codes in the limit of LTE.

3.2. Spectral measurements

3.2.1. Experimental set-up

The experiments presented here were conducted with a 50 kW rf induction plasma torch, shown schematically in Figure 8. The vertical 5-turn coil torch has a 7.5 cm inner diameter and an inner length of 26.5 cm measured between the gas injection plates and the 5 cm diameter exit nozzle, which is located 11 cm above the upper coil. The flow rate of air injected into the torch was approximately 95 slpm, the power delivered to the oscillator plates was 69.0 kW, and the net power deposited into the plasma, determined by calorimetric balance on the water cooling circuit, was about 27 kW.

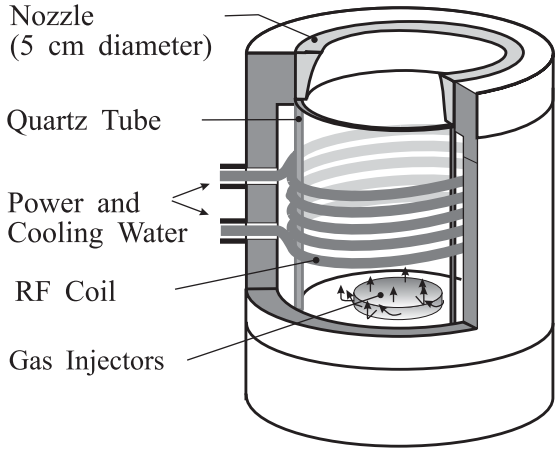


Figure 8. Torch head schematic.

All measurements were made 1 cm downstream of the nozzle exit by means of optical emission spectroscopy, using a SPEX model 750M, 3/4 meter, scanning monochromator fitted with a Hamamatsu model R1104 photomultiplier tube (see Figure 9). Two 1200 lines/mm gratings blazed at 200 and 500 nm were used to cover the spectral range 185-800 nm. The optical train included either two magnesium fluoride lenses (for measurements in the visible) or two spherical mirrors (for measurements in the ultraviolet). The advantage of spherical mirrors over lenses is that they do not create chromatic aberration, which is important to obtain reliable absolute intensity measurements. Absolute intensity calibrations were obtained with two NIST traceable radiance standards: a 1 kW Argon Mini-Arc from Arc Applications Research for wavelengths between 185 and 400 nm, and an Optronics model OL550 tungsten filament lamp between 350 and 800 nm. Data were acquired using a Stanford Research Systems model SR830 lock-in amplifier, and transferred to a laboratory computer for processing. For measurements in the range 400-800 nm, second order light from the region 200-400 nm was rejected by means of a long pass filter with cut-off at 390 nm inserted in the optical train before the PMT detector.

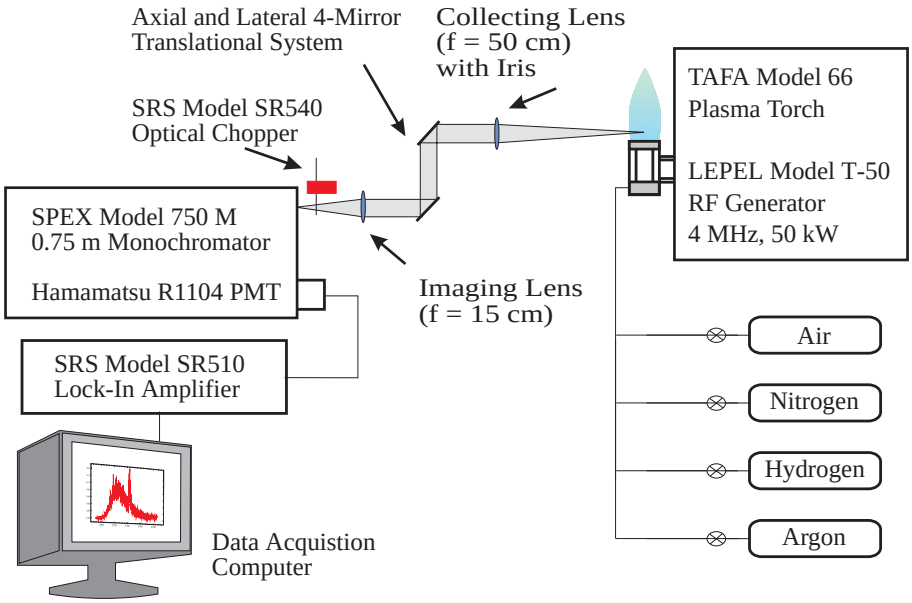


Figure 9. Set-up for emission measurements

3.2.2. Thermodynamic state of the plasma

The thermodynamic characterization of the plasma was the object of studies [32, 59, 60] summarized in this section. As follows from the electron energy equation in the current-free region downstream of the RF coil, the high collision frequency between electrons and heavy particles at atmospheric pressure ensures efficient energy transfer and thus equilibration between the translational modes of electrons and heavy species. Therefore, at the exit of the torch where measurements were made, the plasma is expected to be close to thermal equilibrium, i.e. the free electron and gas kinetic temperatures are essentially equal.

Thermalization of the translational modes of electron and heavy particles is not however a sufficient condition for the populations of internal energy states of atoms and molecules to follow Boltzmann distributions, let alone Boltzmann distributions at a common temperature. For the populations of internal energy states of a thermal plasma to follow Boltzmann distributions at a common temperature, the plasma must also be in chemical equilibrium. Indeed, nonequilibrium concentrations of free electrons can cause departures from equilibrium in the populations of excited internal states of atoms and molecules owing to collisional-coupling between bound and free-electrons [61]. Similarly, nonequilibrium concentrations of atomic species may result in nonequilibrium electronic or vibrational population distributions, particularly for those molecular excited states that are strongly coupled with atomic species via predissociation/inverse predissociation reactions (see Section 5). Thus, the issue of chemical equilibration at the plasma torch exit was carefully examined through modeling of plasma recombination.

The air plasma was generated within the RF induction coil region and measurements were made 1 cm downstream of the nozzle exit, i.e. ~12 cm downstream of the induction region. The characteristic flow time between the induction region and the measurement plane is estimated to be on the order of 10 milliseconds. The degree of chemical equilibration at the measurement location depends on the relative values of the characteristic flow and chemistry times. To determine the characteristic chemistry time, kinetics of recombining air plasmas were modeled with the CHEMKIN solver[62] using the 11-species mechanisms of Dunn and Kang [63], Park [8, 64], and Gupta *et al*. [65]. In the induction region the maximum plasma temperature is estimated [32] to be ~9,000 K, and the concentrations of atoms and electrons are no larger than the corresponding concentrations under chemical equilibrium conditions at 9,000 K. At the exit plane of the torch, the measured plasma temperature varies from ~7,800 K at the center to ~4000 K at outer radii (see Figure 10). Most of the radiation is emitted in the central region at temperatures above 6000 K. We modeled the situation of an air plasma initially in chemical equilibrium at 9000 K forced to recombine as a result of instantaneous cooling to 6,000 K. All three kinetic mechanisms predict that the time required to reach chemical equilibrium at 6,000 K is shorter than one millisecond. Since the characteristic chemical equilibration time is much shorter than the characteristic flow time (~10 ms), flow-induced chemical nonequilibrium at the torch exit is unlikely.

The temperature profile was measured using several techniques. First, we determined "LTE" and "Boltzmann" temperature profiles based on Abel-inverted profiles of the absolute and relative intensity respectively of five atomic oxygen and nitrogen lines. As shown in Figure 10, the LTE and Boltzmann temperature profiles are close from one another. Second, a spatially-resolved rotational temperature profile was obtained by Abel-inverting lateral measurements of the NO γ (0–1) band shape, using the technique proposed by Gomès et al. [66]. The measured

rotational temperature profile, shown in Figure 10, is also in agreement with the electronic temperatures. Third, a vibrational temperature profile was measured from the relative intensities of Abel-inverted lateral profiles of two bandheads of N_2^+ (first negative system), the (0–0) band at 391.4 nm, and the (2–1) band at 356.4 nm. As can be seen from Figure 10, the measured vibrational, rotational, and electronic temperature profiles are to within experimental uncertainty in good agreement with each other. This supports the assumption that internal energy state populations follow a Boltzmann distribution at a common temperature. This common temperature is most accurately characterized by the profile obtained from the 777.3 nm oxygen line because the population of the upper state of this transition is very sensitive to temperature variations owing to the large energy difference relative to the ground state. Thus all spectral simulations presented in the next sections are based on the LTE temperature profile of the 777.3 nm O line.

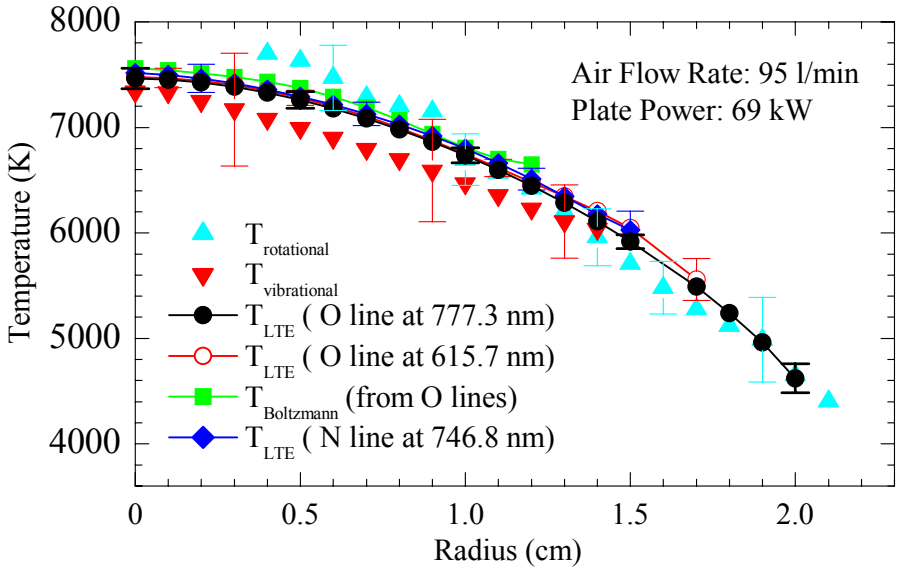


Figure 10. Electronic, vibrational, and rotational temperature profiles in the plasma torch.

3.2.3. Spectral measurements

The line-of-sight emission spectrum measured along the plasma diameter in the spectral range 185 to 800 nm is shown in Figure 11. The monochromator entrance and exit slits were set to 60 and 260 μm, corresponding to a trapezoidal spectral bandpass of base 0.35 and top 0.22 nm. The monochromator scanning speed was 0.2 nm/sec. The accuracy of the calibrated spectra is estimated to be ~10% over the entire spectral range except at short wavelengths below 190 nm where plasma emission is smaller than the signal due to zero-order grating dispersion.

The experimental spectrum contains a wealth of emission features due to electronic band systems of N_2^+, N_2, O_2, NO, and CN, as well as atomic lines of carbon, oxygen, and nitrogen. It can be shown [32] that the range of temperatures at which these various systems emit in

comparable amounts is very narrow and centered around 7500 K. At temperatures above 9000 K over 90% of the power radiated by air plasmas emanates from atomic lines only, whereas at temperatures below 6000 K over 90% of the radiation is emitted by O_2 and NO transitions only. Thus the temperature range of the present work is optimally suited for high temperature air plasma radiation studies. Since the plasma is close to LTE and since the LTE temperature is known accurately, these experimental spectra can be used to benchmark radiation codes.

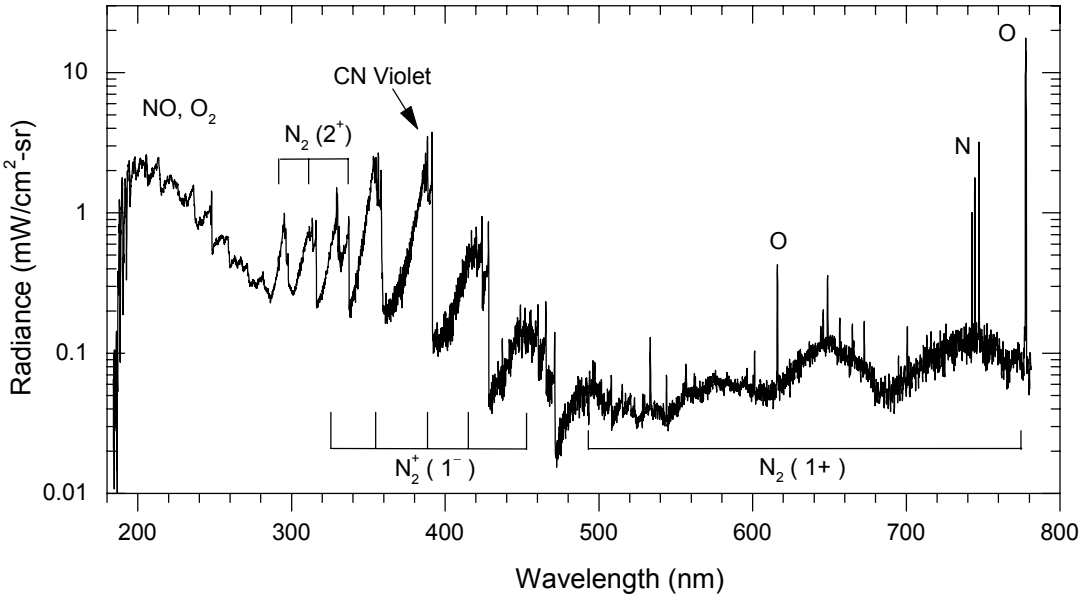


Figure 11. Measured plasma torch emission spectrum. The main emission features are indicated.

3.3. SPECAIR model of the plasma torch emission spectrum

To numerically simulate the measured line-of-sight spectrum, we use the following approach. The plasma is divided into 25 equally spaced concentric rings with uniform thermodynamic properties. In each ring, the translational, rotational, vibrational and electronic temperatures are set equal to the LTE temperature measured from the 777.3 nm oxygen triplet, and the composition is determined assuming chemical equilibrium from a baseline air composition of 78.084% N_2, 20.946% O_2, 0.934% Ar, and 0.033% CO_2. The small amount of atmospheric carbon dioxide is responsible for the intense CN violet bands observed at 380-390 nm and the carbon line at 247.9 nm.

Spectral emission coefficients, $\varepsilon(\lambda)$ (W/cm^3-sr-μm), and spectral absorption coefficients including stimulated emission, $k'(\lambda)$ (cm^{-1}), are computed in 50 segments along the diameter of the plasma. The spectral emission and absorption coefficients are calculated between 185 and 800 nm at spectral intervals of 0.001 nm to resolve the rotational lines whose FWHM is typically about 0.01 nm for the present experimental conditions.

The line-of-sight spectrum $I_{los}(\lambda)$ is determined either by assuming that the medium is optically thin to all radiation, or by solving the radiative transport equation. For optically thin calculations, the spectral emission coefficient in each segment is multiplied by the length x of the segment and the total emission spectrum at the exit of the plasma is obtained by adding the contributions of all segments. Spectral simulations taking into account self-absorption are made by solving the radiative transport equation:

$$\frac{dI(\lambda)}{dx} = \varepsilon(\lambda) - k'(\lambda) I(\lambda). \tag{5}$$

The spectral intensity $I_n(\lambda)$ at the exit of the nth segment is related to the intensity $I_{n-1}(\lambda)$ entering the segment by integrating Eq. (5) over the n^{th} segment (wherein thermodynamic properties are assumed to be uniform):

$$I_n(\lambda) = \frac{\varepsilon_n(\lambda)}{k'_n(\lambda)}\left[1 - \exp\left(-k'_n(\lambda)x\right)\right] + I_{n-1}(\lambda)\exp\left(-k'_n(\lambda)x\right). \tag{6}$$

The quantities $I_n(\lambda)$ are then summed over all segments to provide the line-of-sight emission spectrum $I_{los}(\lambda)$.

The predicted line-of-sight spectrum $I_{los}(\lambda)$ [W/cm^2-sr-μm] is then corrected for absorption by room air due to the bands and continuum of the O_2 Schumann-Runge system over the 5 meter path length separating the plasma from the PMT. Finally, the corrected spectrum $I'_{los}(\lambda)$ [W/cm^2-sr-μm] is convolved with the slit function S(λ):

$$I_{SPECAIR}(\lambda) = \int_0^\infty I'_{los}(\lambda) S(\lambda + \xi) d\xi \ . \tag{7}$$

$I_{SPECAIR}(\lambda)$ has units of W/cm^2-sr and can be directly compared with the experimental spectra.

3.4. Comparison SPECAIR-Experiments

3.4.1. Overview comparison

An overview comparison between experiment and SPECAIR computations is shown in Figure 12. Good agreement is obtained for the position and intensity of molecular and atomic lines. Some spectral features appear to be slightly underpredicted by SPECAIR, for example the N_2^+ (0,0) band at 391.1 nm. It is important to understand that the difference (about 20 %) is well within modeling and experimental uncertainties. For example, the intensity of the oxygen triplet at 777.3 nm and of the N_2^+ first negative band head at 391 nm change by about 20% if the temperature changes by 1%. The remaining intensity differences are therefore not significant. More detailed comparisons between the experimental and simulated spectra are presented in the following subsections.

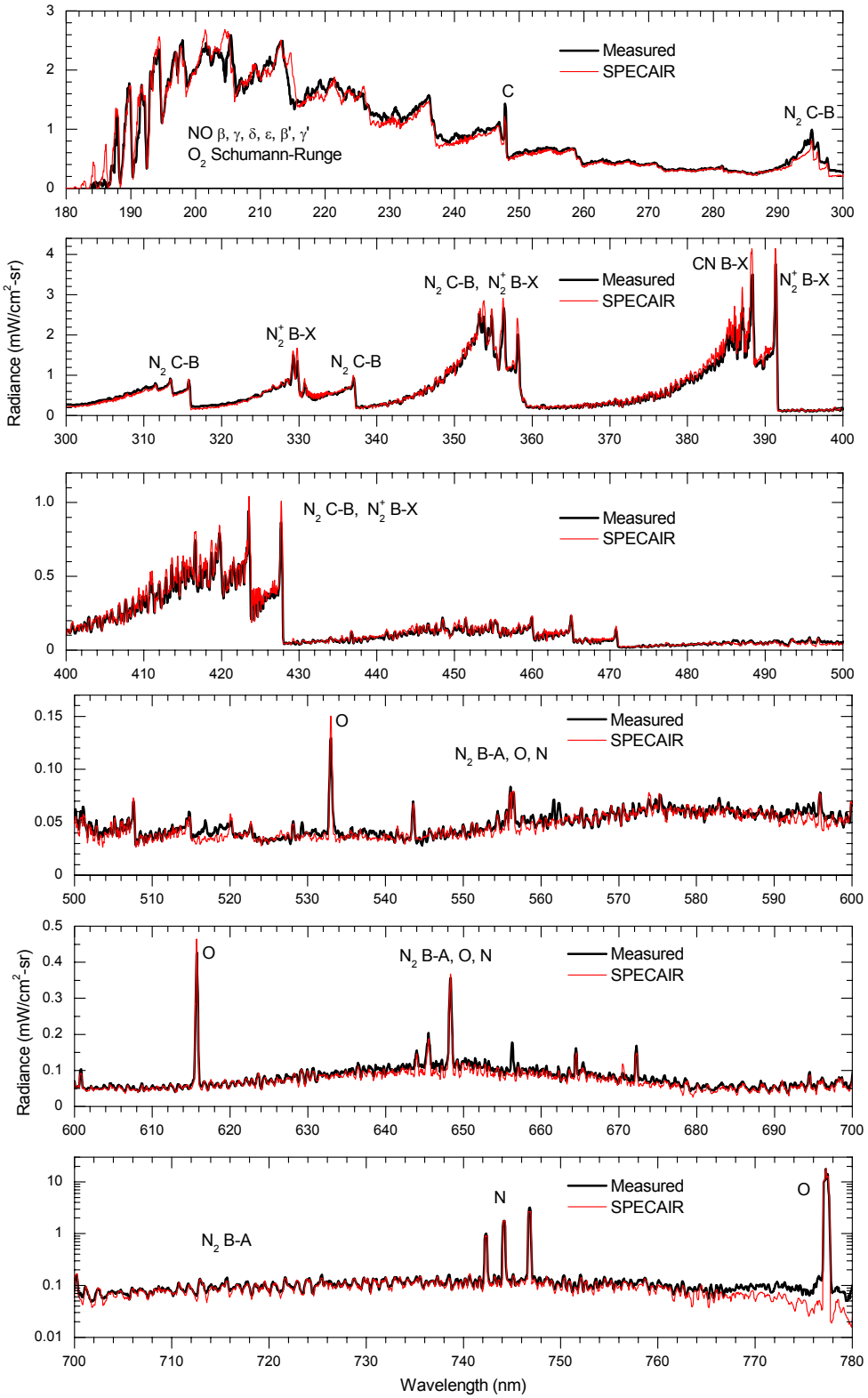


Figure 12. Comparison between the predictions of SPECAIR and the benchmark experimental spectra. (simulations include self-absorption, as well as room air absorption below 200 nm)

3.4.2. Range 185-280 nm

Between 185 and 280 nm, the emission spectrum is dominated by molecular bands of NO and O_2 and by atomic lines of nitrogen, oxygen, and carbon. Below 200 nm, the plasma emission spectrum is partly absorbed by room air in the 5-meter path separating the plasma from the PMT. Room air absorption is mostly due to the O_2 Schumann-Runge bands and continuum.

In the early course of this work [30], comparison of the experimental and NEQAIR spectra showed that the numerical spectrum failed to reproduce experimental observations. Even after replacing the transition probabilities and spectroscopic constants of NO β and γ and O_2 Schumann-Runge with more accurate values, the predicted spectrum still underestimated the experimental spectrum (Figure 14). To improve the model, several radiating systems of NO (NO δ, ε, β′ and γ') were incorporated into SPECAIR [32]. Figure 15-Figure 18 show the effect of incrementally adding these systems. NO δ and ε produce a large amount of radiation in the ultraviolet because their transition strength is approximately 4 times larger than that of NO γ. Considered for the first time in radiation models of high temperature air, NO δ and ε were found to be major radiators in the ultraviolet.

It may appear surprising that NO δ produces any radiation considering that all levels above v=0 and J>4.5 of the emitting $C^2\Pi$ state of this transition predissociate as a result of an interference with the $a^4\Pi$ state of NO (see for example Gadd et al[67]). It can be shown however that if atomic species N and O are in LTE, the rate of inverse predissociation balances the rate of predissociation and therefore the C state of NO is close to LTE as well [32].

Two additional systems of nitric oxide, NO β' and γ', were also incorporated into SPECAIR. These systems contribute less than 3% to the total spectrum above 200 nm. However they have non-negligible contributions in the VUV range 150-200 nm as can be seen from Figure 21. Additional transitions from even higher Rydberg states of NO may be important in the VUV as well. Future radiation code development should include these systems, in particular the NO F-X transition.

The spectrum between 180 and 280 nm features several atomic lines of carbon (247 nm) and oxygen. For optically thin plasmas, the atomic lines below 200 nm produce significant emission (Figure 18). Although these lines are largely self-absorbed, a non-negligible fraction of atomic emission escapes the plasma (Figure 19). However, most of the escaping radiation is absorbed over the 5-m path of room air. In the spectrum shown in Figure 20, the only atomic line emission not absorbed by room air is the carbon line at 247.8 nm.

The final SPECAIR spectrum accounting for both self- and room air-absorption is shown in Figure 20. Self-absorption amounts to about 10-20% for some of the atomic lines and for the intense ultraviolet bands of NO. The spectrum is plotted versus air wavelengths above 200 nm

and vacuum wavelengths below 200 nm. Room air is practically opaque below 185 nm. Between 185 and 280 nm, the experimental and numerical results agree within better than 5%, a value consistent with both experimental and modeling uncertainties. Two anomalies remain around 205 and 215 nm, i.e. near the head of the 2-0 and 1-0 NO gamma bands, where the measured spectrum appears to be affected by an unidentified absorption feature. The origin of this absorption is unknown to us and will require further investigations.

A summary of the optically thin emission spectra of importance in the range 160-280 nm is shown in Figure 21. As can be seen in the figure, NO γ, δ, and ε are major contributors to the molecular radiation in this range, and NO β′ and γ′ radiate in similar proportions as NO β.

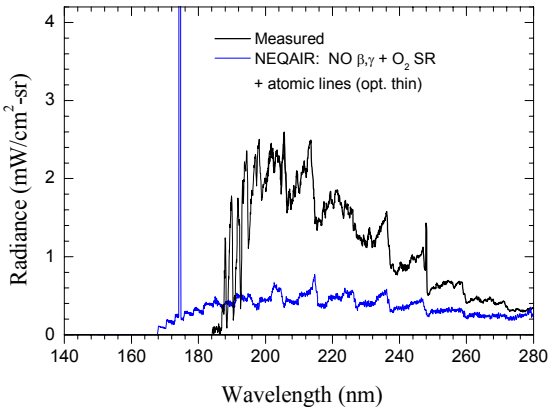


Figure 13. NEQAIR spectrum of NO β, NO γ and O_2 Schumann-Runge, neglecting self-absorption.

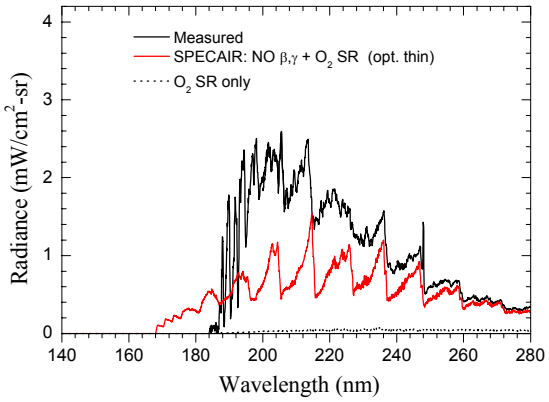


Figure 14. SPECAIR: NO β, NO γ and O_2 Schumann-Runge, neglecting self-absorption.

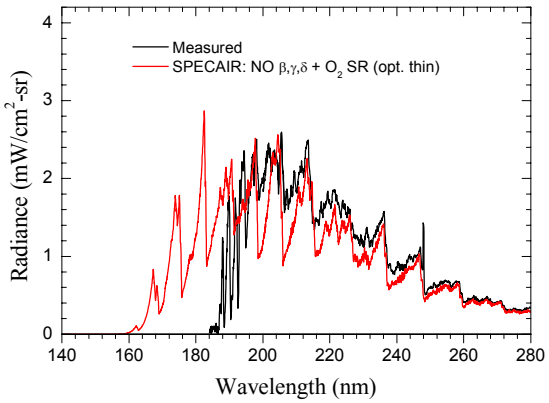


Figure 15. SPECAIR: NO β, γ, δ and O_2 SR, neglecting self-absorption.

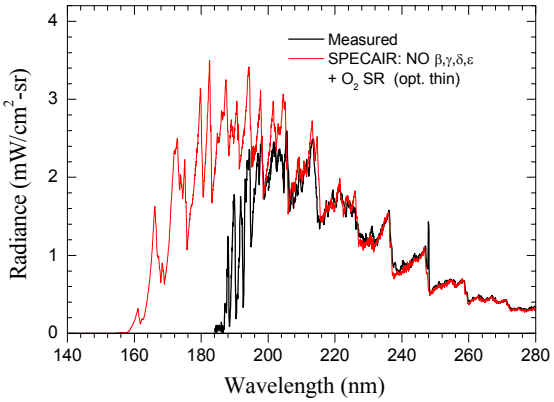


Figure 16. SPECAIR: NO β, γ, δ, ε and O_2 SR, neglecting self-absorption.

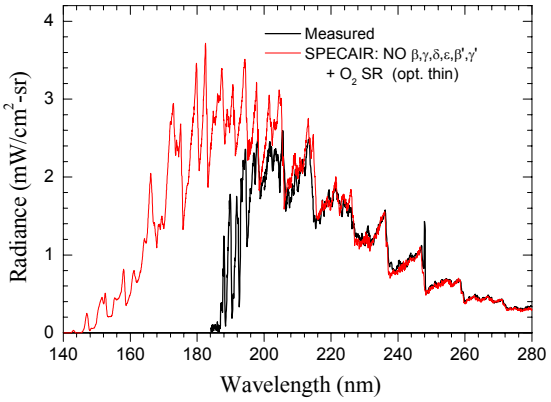


Figure 17. SPECAIR: NO β, γ, δ, ε, β', γ' and O_2 SR, neglecting self-absorption.

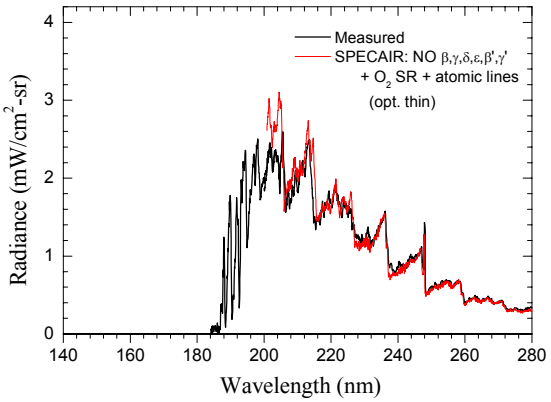


Figure 18. SPECAIR: NO β, γ, δ, ε, β', γ', O_2 SR and atomic lines, neglecting self-absorption.

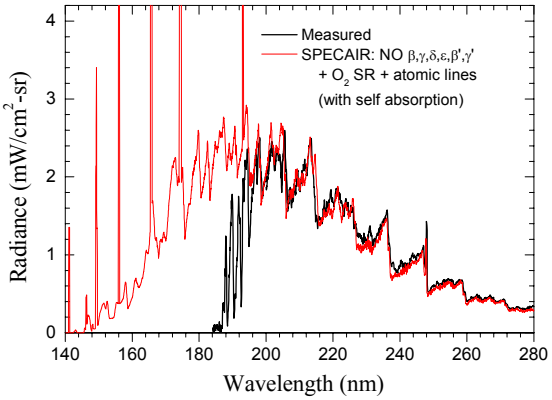


Figure 19. SPECAIR: NO β, γ, δ, ε, β', γ', O_2 SR and atomic lines, including self-absorption within plasma.

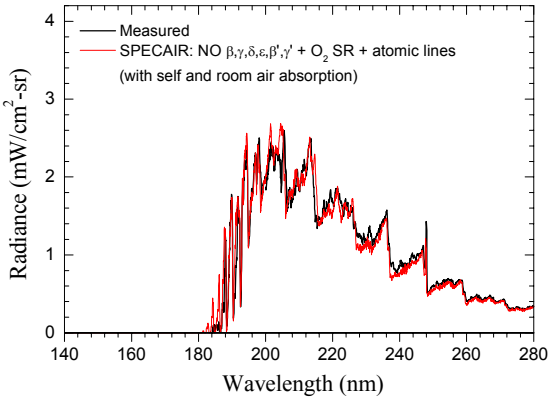


Figure 20. SPECAIR: NO β, γ, δ, ε, β', γ', O_2 SR and atomic lines, including self-absorption within plasma and absorption in 5 m of room air.

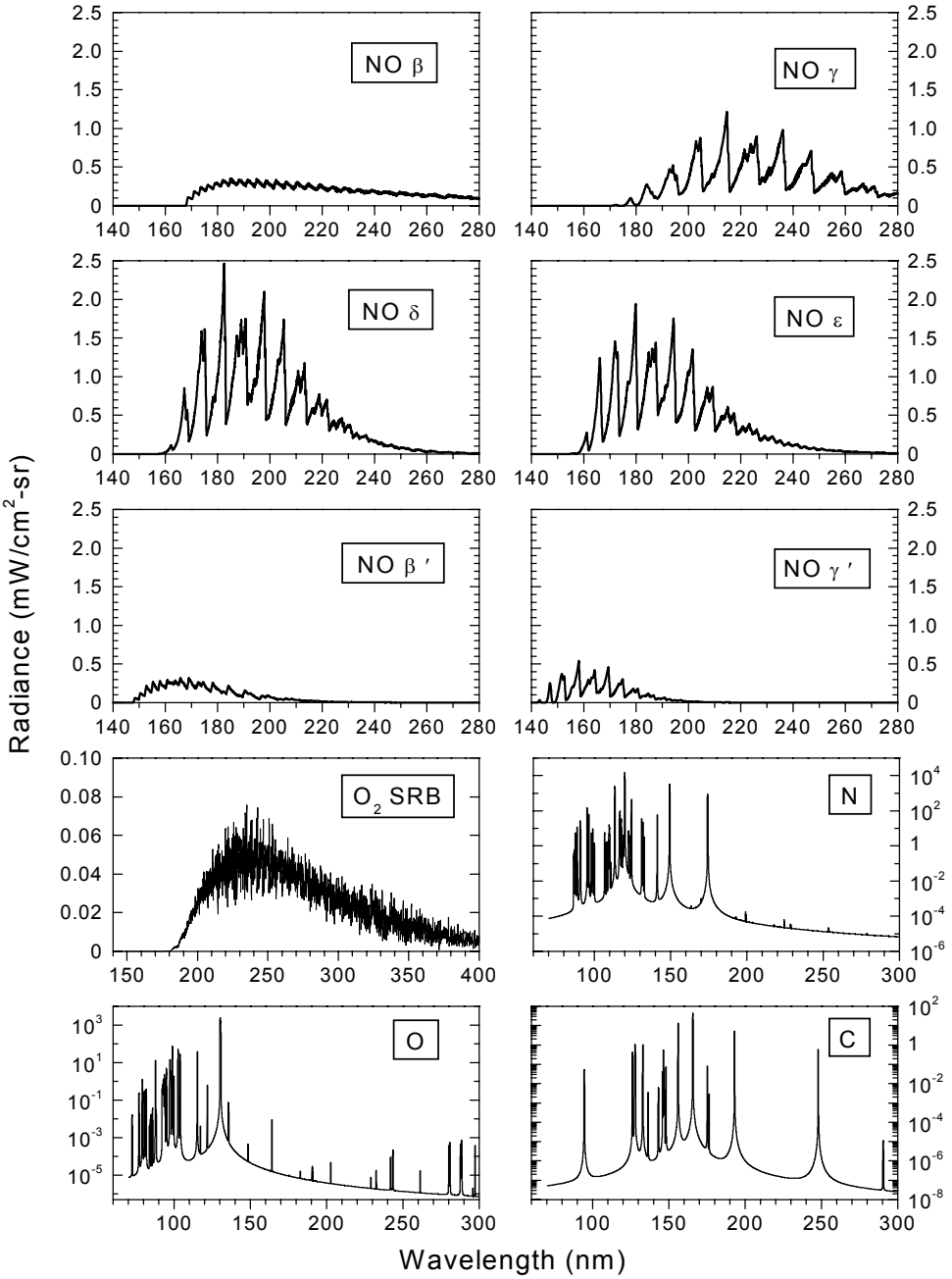


Figure 21. SPECAIR predictions of the radiating systems contributing to the measured plasma torch air spectrum. All spectra were computed assuming optically thin conditions.

3.4.3. Range 280-500 nm

As shown in Figure 22 and Figure 23, the spectral range 280-500 nm is dominated by emission of the second positive system of N_2 (C-B transition), the first negative system of N_2^+ (B-X transition), and the violet system of CN (B-X). In humid air plasmas (or in air mixed with hydrogen), the OH (A-X) and NH (A-X) transitions may also appear around 310 and 330 nm respectively.

In SPECAIR, the spectroscopic models of the first negative system of N_2^+ and of the second positive system of N_2 represent a significant improvement over previously available models. In particular, SPECAIR models perturbations in the rotational lines emanating from levels as high as N = 105 in the array of vibrational bands $0 \le v_X \le 7$ and $0 \le v_B \le 4$ of N_2^+, based on the recent measurements of Michaud *et al* [68, 69]. The capabilities of the model for the analysis of high resolution spectra were recently demonstrated in Ref. [70].

As can be seen from Figure 22, the SPECAIR predictions are in excellent agreement with the measured spectrum except for a discrepancy around 280 nm where the N_2 second positive system does not appear to fully explain the observed radiation. This discrepancy is attributed to the presence of an underlying molecular emission of unidentified origin.

For our experimental conditions, self-absorption by the plasma is small but not negligible: in the spectral range 280-500 nm the SPECAIR spectrum computed by solving the radiative transport equation is approximately 6% times less intense than the optically thin spectrum.

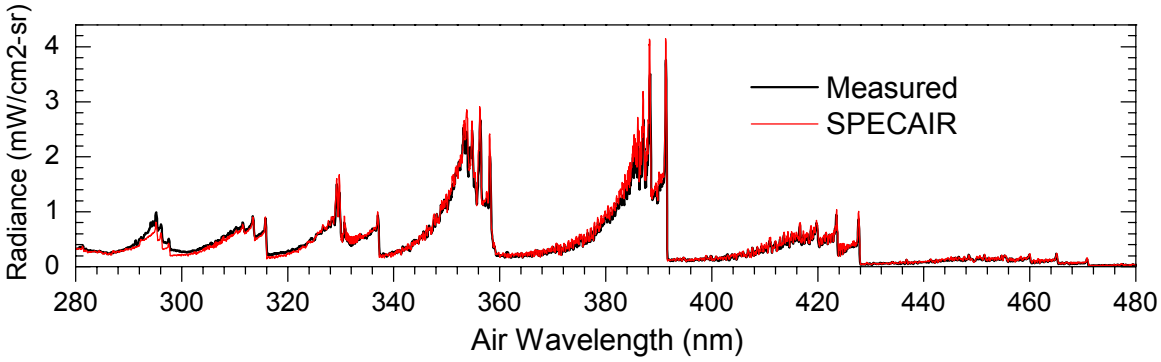


Figure 22. Comparison of SPECAIR and experimental spectra in range 280-480 nm.

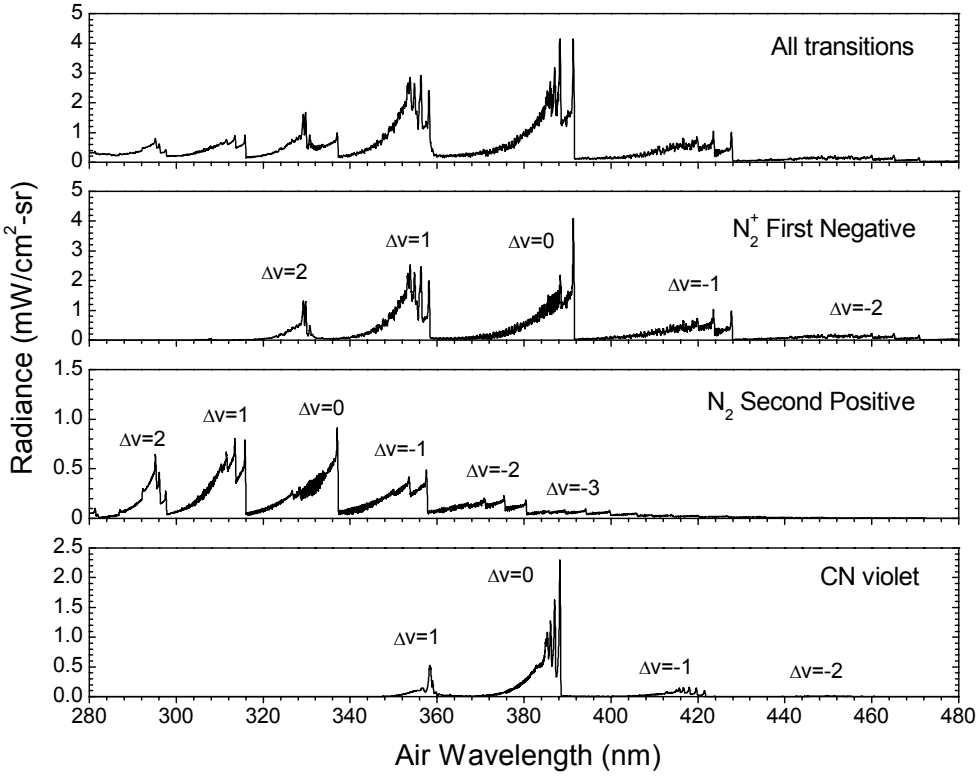


Figure 23. Dominant radiating systems in the range 280-480 nm, as predicted by SPECAIR

3.4.4. Range 500-800 nm

The spectral range 500-800 nm is dominated by emission of the first positive system of N_2 (B-A transition) and atomic lines of nitrogen and oxygen. Several systems of lesser importance underlie the total spectrum, including the Meinel system of N_2^+ (A-X) and the red system of CN (A-X). Figure 24 shows the contributions of these systems to the total spectrum. SPECAIR incorporates a detailed model of the first positive system of N_2, using the spectroscopic models and constants of Roux et al. [51, 52]. The first positive system of N_2 constitutes the dominant part of the spectrum underlying the atomic lines. Figure 25 shows a close-up comparison of the measured spectrum to the predictions of NEQAIR and SPECAIR between 700-750 nm. It is clear that the underlying first positive system is now well modeled.

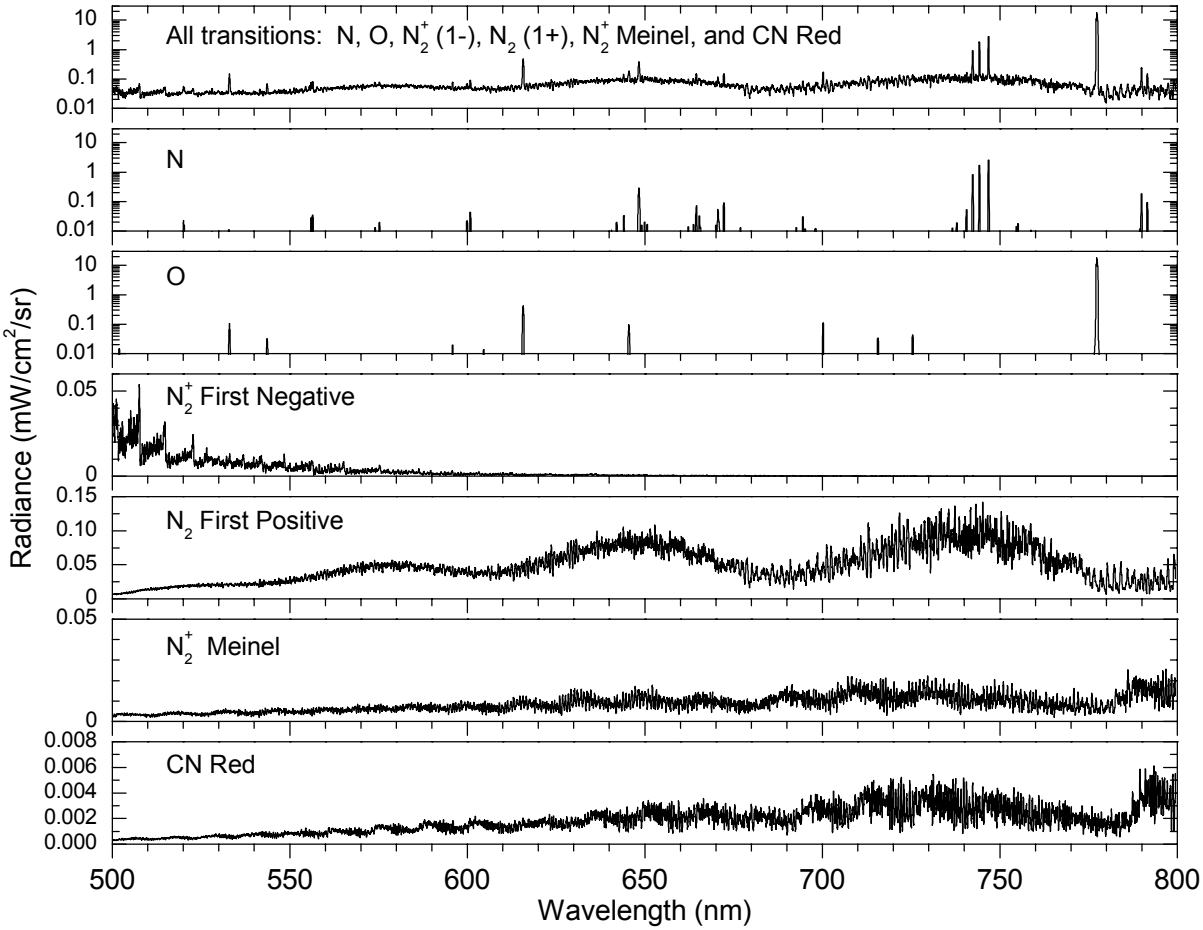


Figure 24. Radiating systems in the range 500-800 nm, as predicted by SPECAIR.

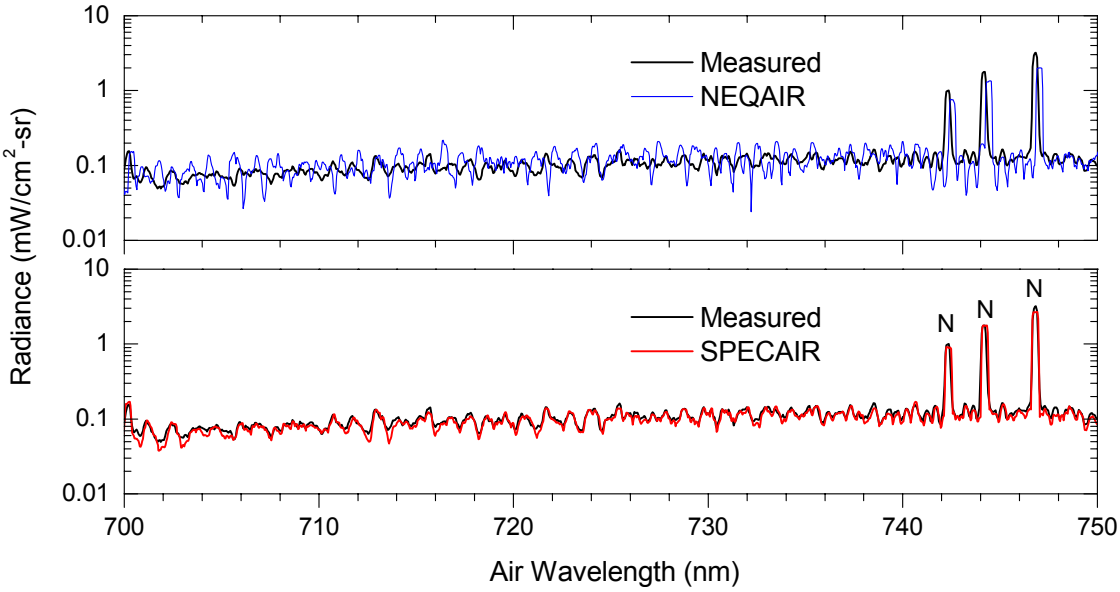


Figure 25. Experimental, NEQAIR and SPECAIR spectra between 700 and 750 nm.

3.4.5. Vacuum Ultraviolet

Although we have not extended our measurements to the VUV below 185 nm, radiation models were incorporated into SPECAIR to estimate the importance of radiative transitions in that range. We already discussed in Section 3.4.2 the various VUV transitions due to atomic species and NO beta, gamma, delta, epsilon, beta prime, and gamma prime. As shown in Figure 21, the NO transitions are responsible for the bulk of molecular emission at wavelengths longer than 140 nm.

At wavelengths below 140 nm, the emission spectrum exhibits several transitions of N_2 including $b^1\Pi_u \rightarrow X^1\Sigma_g^+$ (Birge-Hopfield 1, or BH1), $b'^1\Sigma_u^+ \rightarrow X^1\Sigma_g^+$ (Birge-Hopfield 2, or BH2), $c_4'^1\Sigma_u^+ \rightarrow X^1\Sigma_g^+$ (Carrol-Yoshino, or CY), $c_3{}^1\Pi_u \rightarrow X^1\Sigma_g^+$ (Worley-Jenkins, or WJ), $o_3{}^1\Pi_u \rightarrow X^1\Sigma_g^+$ (Worley, or W), and $e'^1\Sigma_u^+ \rightarrow X^1\Sigma_g^+$. Modeling the radiation due to these transitions is complicated by the strong homogeneous interactions between the emitting states. Homogeneous configuration interactions are between states with the same projected electronic orbital angular momentum Λ, for example either the Rydberg states $b'^1\Sigma_u^+$, $c_4'^1\Sigma_u^+$, and $e'^1\Sigma_u^+$, or the valence states $b^1\Pi_u$, $c_3{}^1\Pi_u$ and $o_3{}^1\Pi_u$. Through these interactions, near-resonant vibrational levels of the interacting electronic states borrow intensity from one another. As shown by Stahel et al. [71], the measured Einstein A coefficient of the b-X(5-0) band is approximately 12 times smaller than if the b(v=5) state were not perturbed. Thus it is clear that homogeneous interactions must be taken into account for these transitions.

In an earlier version of SPECAIR [33], preliminary radiation models were developed for the BH1, BH2, and CY systems, but these models accounted for homogeneous configuration interactions in very approximate manner. In the present work, homogeneous interactions are modeled rigorously with the method of Stahel, Leoni, and Dressler [71], extended to all transitions ending in the first sixteen vibrational levels of the ground state.

Figure 26 shows numerical simulations of the six VUV transitions of N_2. The calculations shown in Figure 26 were performed by assuming the plasma to be optically thin. The optically thin emission spectrum of the combined systems is shown as the upper curve in Figure 27. The lower curve of Figure 27 accounts for self-absorption in the plasma. As can be seen from Figure 27, radiation emitted below 102 nm is almost entirely reabsorbed in the plasma. Above 102 nm, the plasma becomes increasingly optically thin and N_2 emission above 130 nm is predicted to escape at the edges of the plasma. The radiative flux from the center of the plasma to the outer radii is a potentially important transport process. In air plasmas, a large fraction of this escaping radiation is absorbed by the Schumann-Runge continuum of molecular oxygen.

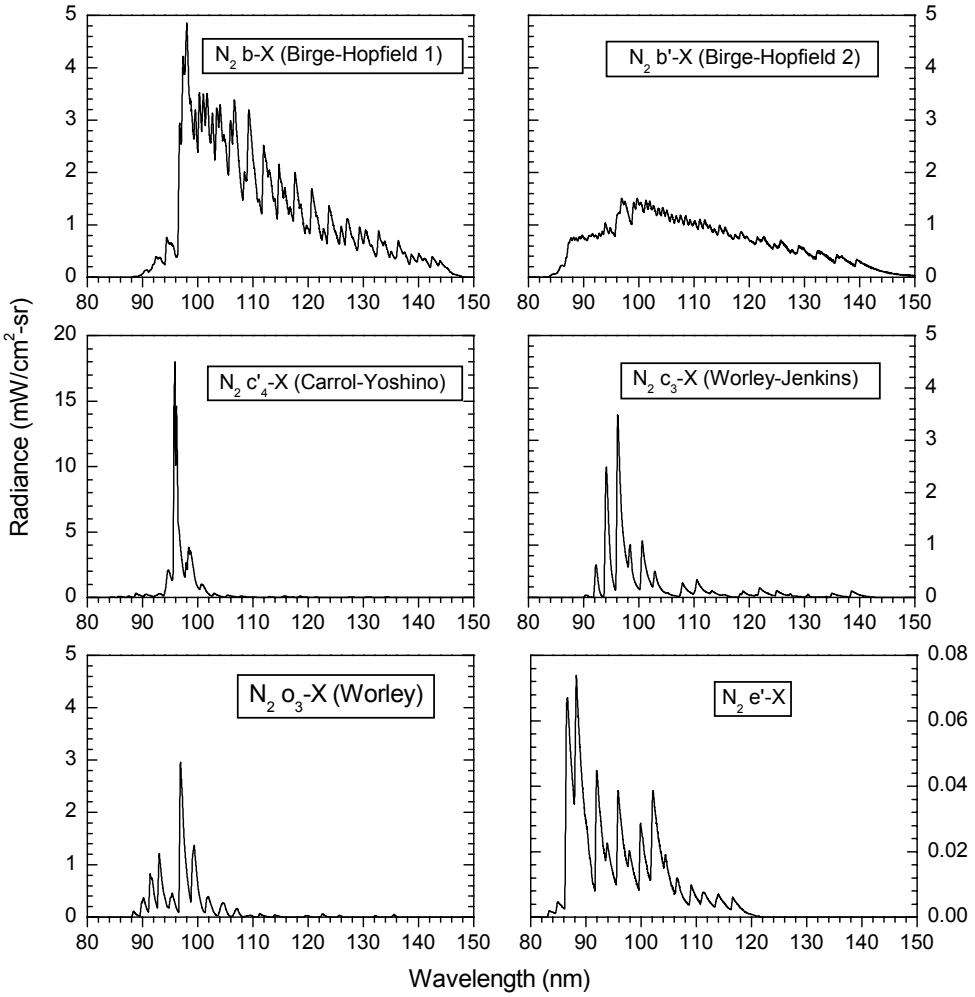


Figure 26. SPECAIR simulations of N_2 VUV transitions for conditions of the plasma torch. All calculations here assume that the plasma is optically thin.

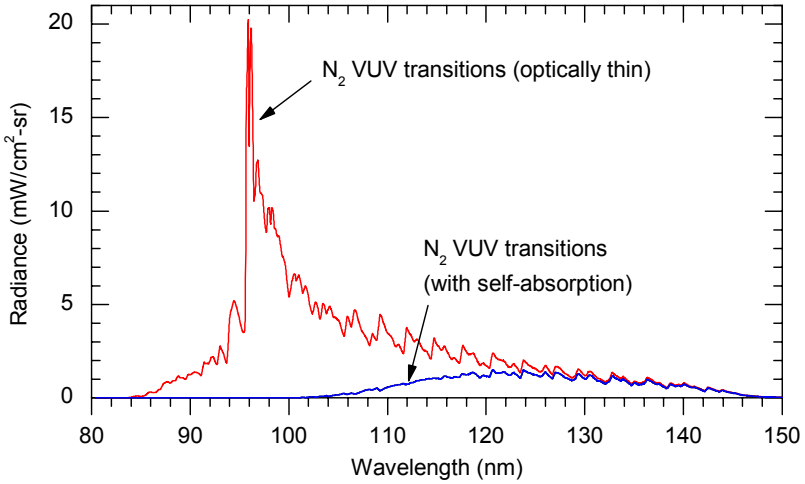


Figure 27. SPECAIR simulations of six VUV systems of N_2. Upper curve: optically thin plasma. Lower curve: considering self-absorption along the plasma diameter.

4. Collisional-radiative modeling of nonequilibrium nitrogen plasmas

4.1. Introduction

To predict nonequilibrium radiation, one needs to predict the populations of the emitting internal levels of atoms and molecules under nonequilibrium conditions. Various forms of nonequilibrium can exist. We distinguish thermal nonequilibrium, where the kinetic temperature T_g of heavy species is different from the kinetic temperature T_e of the electrons, and chemical nonequilibrium. Local Thermodynamic Equilibrium (LTE) corresponds to the case of both thermal and chemical equilibrium.

The nonequilibrium populations of internal energy states can be determined by solving the so-called master equation, which is a system of coupled state-specific rate equations (collisional-radiative model, or CR). While for atomic species it is usually sufficient to consider 10-100 electronic states, for molecular species a much larger number of rovibronic levels must be taken into account. Many CR models [38, 72-75] use the simplifying assumption that the rotational and vibrational energy levels of molecules are populated according to Boltzmann distributions at temperatures T_r and T_v respectively. In these models, the master equation is solved for electronic levels only, with rates obtained by averaging state-specific rates over the rovibrational states of each electronic level. Thus these approaches implicitly assume that departures from Boltzmann distributions in rovibrational states are small.

Departures from Boltzmann distributions, at least in the vibrational levels, are fairly common however. Recent experiments conducted at Stanford University [60] with a nitrogen/argon plasma forced to recombine within 250 μs from a state of equilibrium at a temperature of 7200 K to a state of chemical nonequilibrium at 4720 K have shown that the vibrational levels of certain electronic states, in particular the $B^3\Pi$ of N_2, can strongly depart from a Boltzmann distribution when the concentration of atomic nitrogen is higher than its LTE value. To predict nonequilibrium vibrational populations, a vibrational state-specific collisional-radiative (CR) model must be used. Vibrational state-specific CR models have been developed by several authors [76-82]. No model has been proposed that considers transitions between rotational levels because of the prohibitive computing times required and the lack of knowledge of accurate elementary reaction rates. However, it is often appropriate to consider that the rotational levels follow a Boltzmann distribution because rotational relaxation rates are fast.

In this section, we give an overview of the vibrational state-to-state CR model developed at Stanford for nitrogen plasmas [78-80]. This model is presently being extended to air plasmas [81]. In Section 5, modeling results obtained with the nitrogen CR model are compared with the experimental measurements [60] of N_2 B state vibronic population distributions in a nonequilibrium atmospheric pressure recombining nitrogen plasma.

4.2. Nitrogen CR model

4.2.1. Species and energy levels considered

The species considered in our nitrogen CR model are N, N^+, N_2, N_2^+, and electrons. The internal structure of N is accounted for by using the 22 grouped electronic levels of Park [8]. For N^+, only the ground state is taken into account. The X, A, B, W, B′, and C electronic states of N_2 and the X, A, and B electronic states of N_2^+ are included, and all rovibrational levels belonging to these states are considered up to the dissociation limit. As listed in Table 4, the model takes into account 192 vibronic levels of N_2 and 142 levels of N_2^+.

Table 4. Rovibronic states of N_2 and N_2^+ in the nitrogen CR model. J_{max} is the highest level considered for the ground vibrational level.

N_2			N_2^+		
Electronic state	Vibrational levels	J_{max}	Electronic state	Vibrational levels	J_{max}
$X\ ^1\Sigma_g^+$	0-47	268	$X\ ^2\Sigma_g^+$	0-52	253
$A\ ^3\Sigma_u^+$	0-27	194	$A\ ^2\Pi_u$	0-63	246
$B\ ^3\Pi_g$	0-30	212	$B\ ^2\Sigma_u^+$	0-24	208
$W\ ^3\Delta_u$	0-37	218			
$B'\ ^3\Sigma_u^-$	0-41	225			
$C\ ^3\Pi_u$	0-4	136			

4.2.2. Reactions considered

The present nitrogen CR model considers approximately 11,000 reactions that are summarized in Table 5. These reactions include electron impact ionization, excitation, and dissociation of atoms and molecules, heavy-particle impact dissociation of molecules, as well as electron-impact vibrational excitation of ground state nitrogen (VE transfer), vibrational-translational (VT) and vibrational-vibrational (VV) transfer, charge exchange, dissociative recombination, radiation, and predissociation. Note that because the model neglects several heavy-particle impact processes, it cannot be applied in its present form to plasmas with low ionization degree or high translational temperatures.

Details about the CR model and derivation of the vibrational state-specific rate coefficients are given in Refs. [78-80]. Additional reactions involving air species are given in Ref. [81]. In the following section, we illustrate the derivation of vibrational state-specific rate coefficients with the example of electron-impact ionization of ground state N_2.

Table 5. Reactions considered in the nitrogen CR model. X stands for the ground electronic state of a given species. Y", Y' refer to any electronic state of molecules. Z", Z' refer to any electronic state of atoms. M stands for any heavy collider (N, N^+, N_2, or N_2^+).

Reaction	Cross-section or rate coefficient data	Remarks
Ionization		
$N(Z")+e \leftrightarrow N^+(X)+e+e$	Drawin [83]	
$N_2(Y",v")+e \leftrightarrow N_2^+(Y',v')+e+e$	BEB [84]	X→X, X→A, A→A, B→X, W→A, B'→A, C→B
Dissociation		
$N_2(X,v")+e \leftrightarrow N(X)+N(X)+e$	Majeed [85]	Ground state only
$N_2(X,v")+M \leftrightarrow N(X)+N(X)+M$	Park [8]	M=N or N_2
$N_2(Y",v")+M \leftrightarrow N(Z)+N(Z')+M$	V-T and V-V transfer to the last vibrational level below dissociation limit	M=N, N^+, N_2, N_2^+ Y"=A, B, W, B', C
$N_2^+(Y",v")+M \leftrightarrow N(Z)+N^+(X)+M$		M=N, N^+, N_2, N_2^+ Y"=X, A, B
Dissociative recombination		
$N_2^+(X,v")+e \leftrightarrow N(X)+N(X)$	Peterson [86]	Ground state only
Charge exchange		
$N_2(X,v")+N^+(X) \leftrightarrow N_2^+(X,v')+N(X)$	Stebbings [87]	Ground state only
Electronic excitation		
$N(Z")+e \leftrightarrow N(Z')+e$	Park [8]	
$N_2(X,v")+e \leftrightarrow N_2(Y',v')+e$	Cartwright [88]	Y'=A, B, W, B', C
$N_2(Y",v")+e \leftrightarrow N_2(Y',v')+e$	Seaton [89], Drawin [83]	Y, Y'=A, B, W, B', C
$N_2^+(Y",v")+e \leftrightarrow N_2^+(Y',v')+e$	Seaton [89], Drawin [83]	Y, Y'=X, A, B
Vibrational excitation		
$N_2(X,v")+e \leftrightarrow N_2(X,v')+e$	Kazansky [90] (VE)	Ground state only
$N_2(Y",v")+M \leftrightarrow N_2(Y,v+1)+M$	SSH model (VT)	M=N, N^+, N_2, N_2^+
$N_2^+(Y",v")+M \leftrightarrow N_2^+(Y,v+1)+M$	SSH model (VT)	M=N, N^+, N_2, N_2^+
$N_2(X,v_1)+N_2(X,v_2) \leftrightarrow N_2(X,v_1-1)+N_2(X,v_2+1)$	SSH model (VV)	Ground state only
$N_2^+(X,v_1)+N_2^+(X,v_2) \leftrightarrow N_2^+(X,v_1-1)+N_2^+(X,v_2+1)$	SSH model (VV)	Ground state only
Predissociation		
$N_2(B,12\leq v\leq 18) \leftrightarrow N(X)+N(X)$	Geisen [91]	
$N_2(C,v=4) \leftrightarrow N(X)+N(X)$		Equilibrium with N(X)
Radiation		
$N(Z') \leftrightarrow N(Z")+h\nu$	Park [8]	
$N_2(Y',v') \leftrightarrow N_2(Y",v")+h\nu$	Laux [53]	
$N_2^+(Y',v') \leftrightarrow N_2^+(Y",v")+h\nu$	Laux [53]	

4.2.3 Example of rate coefficient calculation: N_2 ground state ionization by electron impact

To illustrate the principle of vibrational level specific rate coefficient calculations, we discuss here in some detail the case of electron-impact ionization of ground state N_2. We begin by considering the elementary ionization reaction between rovibronic level X,v",J" of N_2 to level A,v',J' of N_2^+.

$$N_2\,(X,v",J") + e \rightarrow N_2^+\,(A,v',J') + e + e$$

We first determine the rate coefficient of this elementary reaction, then we will average the elementary rate coefficients over all initial and final rotational levels of (X,v") and (A,v') in order to obtain the vibrational state-specific rate coefficient.

Elementary rate coefficients

The rate coefficient of electron-impact ionization of N_2 in rovibronic level (X,v",J") producing N_2^+ in rovibronic level (A,v',J') can be written as:

$$K_{N_2Xv"J"}^{N_2^+Av'J'}(T_e) = \frac{8\pi}{\sqrt{m_e}} \frac{1}{(2\pi k T_e)^{3/2}} \int_0^{+\infty} \varepsilon \sigma_{N_2Xv"J"}^{N_2^+Av'J'}(\varepsilon) \exp\left(-\frac{\varepsilon}{kT_e}\right) d\varepsilon \tag{8}$$

where $\sigma_{N_2Xv"J"}^{N_2^+Av'J'}(\varepsilon)$ is the cross-section of the elementary reaction, m_e is the electron mass, and ε the electron energy. In Equation (8), we have implicitly assumed that the electrons have a Maxwellian energy distribution at temperature T_e. (T_e is the kinetic temperature of the electrons, and is not to be confused with the electronic temperature, noted T_{el} earlier in this lecture, that characterizes a Boltzmann distribution of the electronic levels.) All rate coefficients of the CR model assume Maxwellian energy distributions for electrons and heavy species.

Following Park [8], we consider that the Franck-Condon principle holds for transitions in molecules caused by collisions with electrons, and that no change in rotational quantum number occurs as a result of such collisions. Accordingly, we write the elementary cross-section of ionization from rovibronic level (X,v",J") of N_2 to rovibronic level (A',v',J') of N_2^+ as:

$$\sigma_{N_2Xv"J"}^{N_2^+Av'J'} = q_{Xv"}^{Av'}\ \delta_J^{J'}\ \chi\left(\varepsilon, \Delta E_{Xv'J'}^{Av'J'}\right) \tag{9}$$

where $q_{Xv"}^{Av'}$ designates the Franck-Condon factor, $\Delta E_{Xv"J"}^{Av'J'}$ the ionization energy, and $\delta_{J"}^{J'}$ is equal to 1 if J" = J' and to 0 otherwise. The reduced cross-section $\chi(\varepsilon, \Delta E_{Xv"J"}^{A'v'J'})$ is calculated with the Binary-Encounter-Bethe (BEB) model of Hwang *et al.* [84], which provides ionization cross-sections within 15% of experimental values for a wide variety of atoms and molecules. The BEB expression is:

$$\chi\left(\varepsilon, \Delta E_{Xv'J'}^{Av'J'}\right) = 4\pi a_0^2 N \left(\frac{R}{\Delta E_{Xv'J'}^{Av'J'}}\right)^2 \frac{1}{t+u+1}\left[\frac{\ln t}{2}\left(1-\frac{1}{t^2}\right)+1-\frac{1}{t}-\frac{\ln t}{t+1}\right] \tag{10}$$

where R is the Rydberg constant (13.61 eV), a_0 is the Bohr radius (0.5292 Å), N is the electron occupation number in the shell from which ionization takes place, t stands for $\varepsilon/\Delta E^{Av'J'}_{Xv"J"}$ where ε is the kinetic energy of the electron, and u stands for $U/\Delta E^{Av'J'}_{Xv"J"}$ where U is the average kinetic energy of a bound electron in the shell. The values of N and U are given by Hwang et al. for several molecular orbitals of N_2 and O_2.

Vibrational state-specific rate coefficients

To obtain the vibrational state-specific rate coefficient, we sum the elementary rate coefficients over all final rotational levels, and we average over the distribution of initial rotational levels. We assume that the initial rotational levels follow a Boltzmann distribution at rotational temperature T_r, which is a reasonable approximation for many molecules of interest (except the hydrides) owing to fast collisional relaxation of the rotational levels. The vibrational state specific rate coefficient is then:

$$K^{N_2^+Av'}_{N_2Xv"}(T_e,T_r)=\frac{1}{Q^{N_2Xv"}_{rot}(T_r)}\times\sum_{J"}(2J"+1)\exp\left[-\frac{F_{N_2Xv"}(J")}{kT_r}\right]\sum_{J'}K^{N_2^+Av'J'}_{N_2Xv"J"}(T_e) \qquad (11)$$

where $Q^{N_2,X,v"}_{rot}$ is the rotational partition function of N_2 in level X,v", and $F_{N_2Xv"}(J")$ is the rotational term energy of level J". The reverse rates are determined by detailed balance.

5. Application of the CR model to the analysis of a nonequilibrium recombining nitrogen plasma

5.1. Nonequilibrium factors

In this section, we consider the case of a plasma in thermal equilibrium and chemical nonequilibrium. Thermal equilibrium means that all species have equal kinetic temperatures, thus $T_e = T_g = T$. Chemical nonequilibrium implies that the chemical species are under- or overpopulated with respect to their equilibrium concentration at T. It is convenient to define nonequilibrium factors ρ_S as:

$$\rho_S=\frac{[S]}{[S]^{eq}} \qquad (12)$$

where $[S]$ and $[S]^{eq}$ stand respectively for the actual and equilibrium (at temperature T) number density of species or energy level S. A nonequilibrium factor greater than unity implies that the species or state is overpopulated with respect to equilibrium at temperature T. Accordingly, we refer to overpopulation and underpopulation factors of the given state or species.

5.2. Recombining nitrogen plasma experiment

Experiments were conducted at Stanford [60] with a recombining atmospheric pressure nitrogen plasma. In these experiments, a mixture of ~100 slpm N_2, ~50 slpm argon, and ~2.3 slpm H_2 was inductively heated with a 50 kW RF plasma torch. Argon was added to stabilize the torch operating conditions, and H_2 was added for purposes of electron density measurement from the Stark-broadened H_β line. The experimental set-up is shown in Figure 28. The plasma produced by the torch was accelerated to a velocity of ~1 km/s by passing through a 1 cm diameter torch exit nozzle. At the exit of the nozzle, the temperature profile was measured from the absolute intensity of atomic lines of nitrogen at 746.8 nm. The centerline temperature was found to be approximately 7200 K. The plasma was then rapidly cooled (within ~250 μs) by flowing through a 15 cm-long water-cooled modular brass test-section.

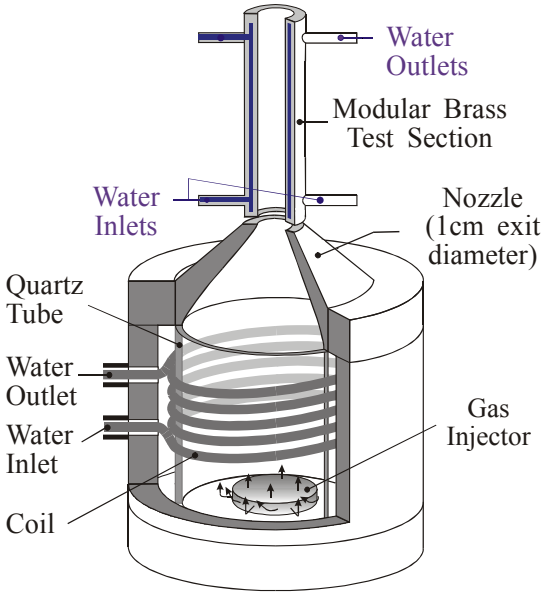


Figure 28. Schematic cross-section of torch head with test-section.

At the exit of the 15-cm test-section, the temperature profile was measured from the N_2^+ first negative system, as described in Ref. [60]. The centerline temperature was found to be 4720±100 K. (Subsequent measurements [70] using rotational lines of the N_2^+ first negative system yielded a centerline temperature of 4850±100 K). In LTE at 7200 K, the plasma composition is 55% N, 19% N_2, and a balance of argon and hydrogen. In LTE at 4720 K, the composition would be 63% N_2, 1.8% N, with a balance of argon and hydrogen. However, because the plasma residence time is shorter than the characteristic time of atomic nitrogen recombination, atomic nitrogen recombination tends to freeze and it is expected that the atomic nitrogen population at the 15-cm test-section exit will be significantly higher than the LTE value.

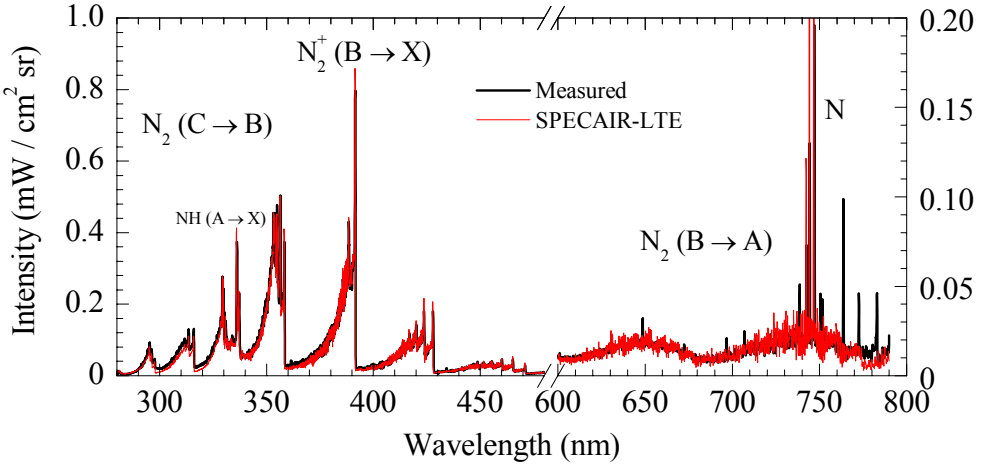


Figure 29. Measured and computed LTE spectra of the nitrogen/argon plasma at the nozzle exit.

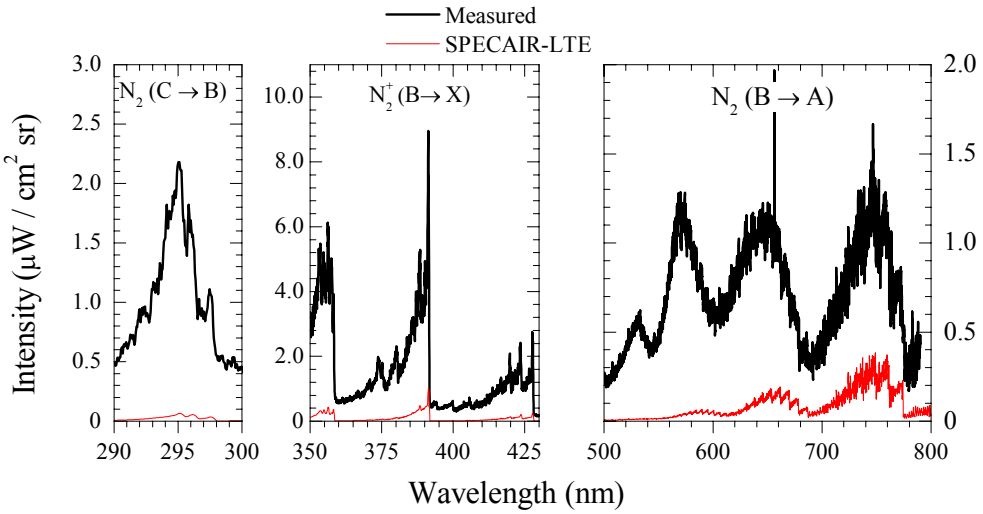


Figure 30. Measured and computed LTE spectra of the nitrogen/argon plasma at 15 cm downstream of nozzle exit.

Absolute emission spectra between 280 and 800 nm were measured both at the nozzle exit and at the test-section exit. These spectra are compared with LTE spectra calculated with SPECAIR using the measured gas temperature profiles. At the nozzle exit the measured and LTE spectra are in close agreement (see Figure 29), which supports the existence of near-LTE conditions at the nozzle exit. At the test-section exit, on the other hand, the measured spectrum is much more intense than the computed LTE spectrum (see Figure 30). The differences in the range 500-800 nm indicate that the vibrational levels of the N_2 B state depart from a Boltzmann distribution. The nonequilibrium vibrational population distribution can be inferred by multiplying the equilibrium populations of individual vibrational levels by nonequilibrium factors chosen so as to match the measured spectrum (see Figure 31). The measured distribution of nonequilibrium population factors is shown in Figure 32. In this graph, a Boltzmann distribution at T_v= 4720 K would be represented by the straight line ρ_v=1. It is clear that the

measured distribution is non-Boltzmann, with a marked peak at v=13. In the rest of the lecture, we concentrate on understanding and modeling the nonequilibrium vibrational population distribution of the B state of N_2.

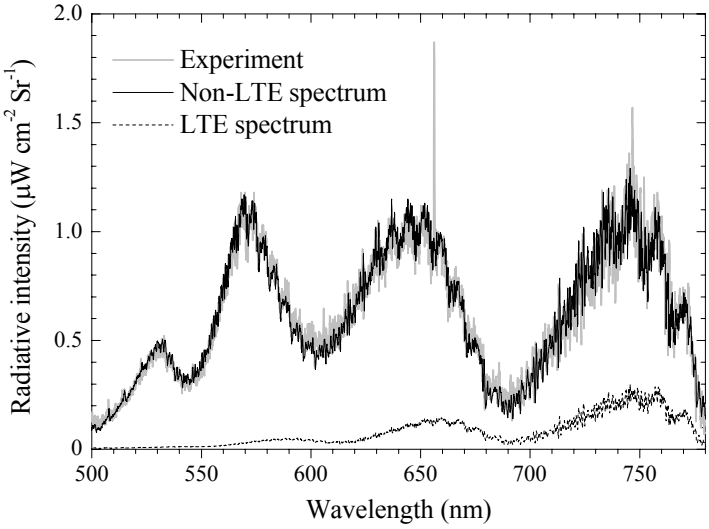


Figure 31. Radiative intensity emitted by the N_2 B-A system at the 15-cm test-section exit: Measurements, LTE SPECAIR spectrum, and non-LTE SPECAIR spectrum obtained with the overpopulation factors of Figure 32.

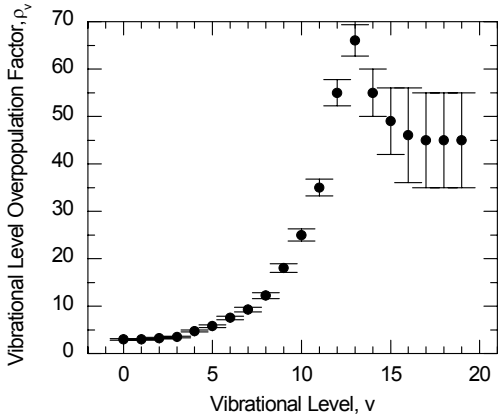


Figure 32. Measured N_2 B state vibrational overpopulation factors in the recombining N_2/Ar plasma.

5.3. Analysis of the recombination experiments with the nitrogen CR model

The nitrogen CR model is used in this section to analyze the recombining nitrogen plasma experiments. We are particularly interested in the nonequilibrium vibrational distribution of the B state of N_2. Argon is not included in the CR model, but it is likely that reactions with argon do not significantly affect the population of the N_2 B state. We consider therefore the case of a pure nitrogen plasma in chemical nonequilibrium. The CR model calculations are performed by making use of the quasi-steady-state (QSS) approximation, which assumes that all excited levels

of atoms and molecules are in steady-state, and equations relative to ground levels are replaced with mass conservation equations.

The input parameters of the model are the temperature $T = 4720$ K, the pressure $p = 1$ atm, and the concentrations of the different species, listed in Table 6, at the exit of the 15-cm test-section. The electron number density was measured [60] from the Stark-broadened H_β line and found to be 7.3×10^{13} cm^{-3}, a factor 180 times larger than the LTE electron concentration at 4720 K. The N atom overpopulation factor (recall that we expect an overpopulation of nitrogen atoms owing to finite nitrogen recombination rate) has been adjusted to obtain the best possible agreement with the peak of the distribution at v=13. Best agreement is obtained with $\rho_N = 8.1$). The concentrations of N^+ and N_2^+ have little influence on the N_2 B state population. Nevertheless, they have been chosen in such a way that the plasma is electrically neutral and that the charge exchange reaction $N_2 + N^+ \leftrightarrow N_2^+ + N$ is balanced.

Table 6. Species concentrations used to simulate the recombining nitrogen plasma conditions at exit of 15-cm test-section.

S	$[S]^{eq}$ (cm^{-3})	[S] (cm^{-3})	ρ_S
N	1.8×10^{16}	1.5×10^{17}	8.1
N^+	4.8×10^{10}	3.8×10^{13}	~800
N_2	1.5×10^{18}	1.5×10^{18}	1
N_2^+	3.5×10^{11}	3.5×10^{13}	100
e	4.0×10^{11}	7.3×10^{13}	180

The experimental vibrational overpopulation factors are plotted in Figure 33 together with three calculation results of the CR model with different values of a few controlling rates. The curve labeled "CR model" was obtained using the baseline rate coefficients of the CR model. This calculation reproduces the general shape of the experimental curve, with a peak at v = 13, but predicts larger overpopulation factors at v's above and below 13.

We examine the sensitivity of the predictions by varying selected rates. Curve (a) was calculated by multiplying the N_2 (X-A) and N_2 (X-B) excitation and de-excitation rates by a factor of 4, and by dividing the predissociation rate of level N_2 (B,v = 12) by a factor of 5. Note that the value of the N_2 (B,v = 12) predissociation rate used in the CR model is an estimate based on the value measured by Geisen *et al.* [91] for v = 13, so that the foregoing adjustment to the rate is reasonable. Similarly, the multiplicative factor of 4 for the X-A and X-B excitation rates is not unreasonable, given the uncertainty on cross-sections for these reactions [92]. With these modified rates, good agreement is obtained with the experimental curve for v=0-13.

Curve (b) presents another calculation in which the rates are modified as in curve (a) and predissociation of levels $v \geq 14$ is neglected. Better agreement with the experimental curve is

now obtained for the high-lying levels $v \geq 14$. This result may suggest that the predissociation rates of levels $v \geq 14$ are overestimated in the model, but it may also be due to uncertainties on other rates. The SSH-based VT transfer rate, for instance, may be somewhat inaccurate for the high lying levels, and multi-quantum jumps may have to be considered. Moreover, the experimental uncertainty on the overpopulation factors of high-lying levels is quite large (see Figure 32) because these levels contribute little to the total emission of the first positive system of N_2.

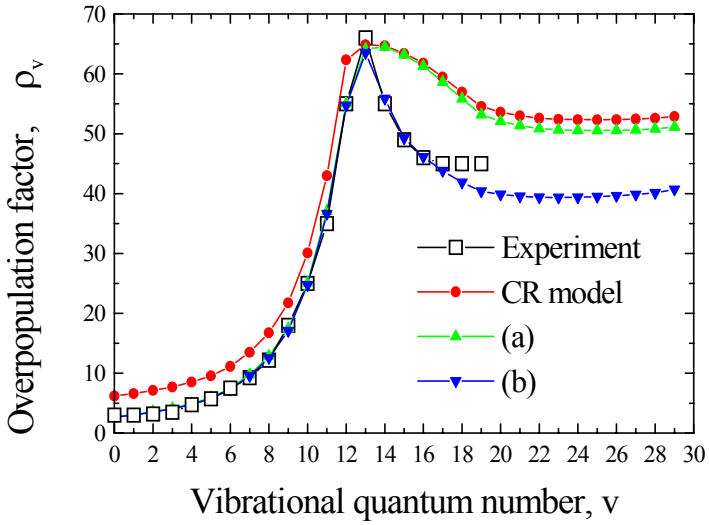


Figure 33. Vibrational overpopulation factors of the N_2 B state. CR model calculation performed with $T = 4720$ K, $p = 1$ atm, $\rho_e = 180$, $\rho_N = 8.1$. (a): CR model with N_2 (X-A) and N_2 (X-B) electron-impact excitation rates multiplied by 4 and the N_2 (B,v=12) predissociation rate divided by 5. (b): same as (a) without predissociation of levels v≥14 of N_2 (B).

Despite the lingering uncertainties on the shape of the vibrational population distribution, the results obtained with the baseline CR model reproduce the observed nonequilibrium distribution reasonably well. The most important result of the analysis is that vibrational level v=13 of the B state of N_2 appears to be fully coupled to the atomic species by predissociation and inverse predissociation. This can be seen by writing the steady-state rate equation for the population of N_2, B, v=13:

$$\frac{dn_{N_2,B,13}}{dt} = 0 = -n_{N_2,B,13}\left\{k^{pred}_{v=13} + \sum_{v''} A_{13v''} + n_M\left(k^{13\to14}_{VT} + k^{13\to12}_{VT}\right) + n_e k^e_{ion} + \sum_{Y=X,A,B',W,C} n_e k^e_{B,13\to Y}\right\}$$
$$+ n_N^2 k^{inv.pr.}_{v=13} + \sum_{Y',v'} n_{N_2,Y',v'} A_{v'13} + n_{N_2,B,14} n_M k^{14\to13}_{VT} + n_{N_2,B,12} n_M k^{12\to13}_{VT} + n_e^2 n_{N_2^+} k^e_{rec} + \sum_{Y=X,A,B',W,C} n_Y n_e k^e_{Y\to B,13} \quad (13)$$

The numerical values of the depleting terms that appear in the first bracket, as calculated with the CR model, are listed in Table 7. It can be seen from the table that the predissociation term is about 30 times larger than the sum of the other depletion terms. Similarly, it can be

shown that the largest term in the processes populating B,v=13 is the inverse predissociation term. It follows that at steady-state Equation (13) can be approximated by:

$$n_{N_2,B,13} k_{\mathrm{v=13}}^{pred} \approx \left(n_N\right)^2 k_{\mathrm{v=13}}^{inv.pred} \tag{14}$$

Using superscript *eq* to designate equilibrium concentrations, we also have the following relation:

$$n_{N_2,B,13}^{eq} k_{\mathrm{v=13}}^{pred} = \left(n_N^{eq}\right)^2 k_{\mathrm{v=13}}^{inv.pred} \tag{15}$$

Dividing Equation (14) by Equation (15), we obtain:

$$n_{N_2,B,13} \Big/ n_{N_2,B,13}^{eq} \approx \left(n_N \Big/ n_N^{eq}\right)^2$$

which using nonequilibrium factor notation can finally be written as:

$$\boxed{\rho_{N_2,B,13} \approx \rho_N^2} \tag{16}$$

Equation (16) expresses a very interesting relation, namely that the overpopulation of the $N_{2,B,v=13}$ state is approximately equal to the square of the overpopulation factor of atomic nitrogen in the ground state. This relation means that it is possible to use emission spectroscopy to infer ground state atomic nitrogen concentrations. For our experimental conditions, the overpopulation factor of v=13 is measured to be $\rho_{N2,B,\ v=13} = 66\pm4$. Thus the overpopulation of nitrogen atoms is approximately 8.1±0.3. At 4720±100 K, the equilibrium concentration of nitrogen atoms in the nitrogen/argon plasma mixture is $1.8\pm0.4\times10^{16}$ cm^{-3}. Multiplying this number by the measured overpopulation factor ρ_N, we infer a nonequilibrium nitrogen atom concentration of $1.5\pm0.4\times10^{17}$ cm^{-3}. Note that relation (16) is also valid at pressures lower than one atmosphere because the various depletion terms decrease with decreasing pressure and therefore become even more negligible relative to the rate of predissociation.

The CR model also predicts the populations of additional vibronic states. Figure 34 shows the vibrational overpopulation factors of the X, A, B, W, B′, and C states of N_2 as a function of the vibrational quantum number v, calculated with the same modified rates as curve (a) of Figure 33. All states have overpopulation factors of low-lying levels in the range 2 to 4, which indicates that they are in partial equilibrium with each other. The overpopulation factor of the X, A, and C states increase steadily with v to reach values close to that corresponding to dissociation equilibrium. The W state overpopulation curve exhibits two inflexion points, and the B′ state overpopulation curve has a local maximum similar to that of the B state. These behaviors are caused by collisional coupling with predissociating levels of the B state.

Table 7. Reaction rates (normalized by the population of $n_{N2,B,v=-13}$) for the major depletion mechanisms of N_2 (B,v=13) in a nonequilibrium nitrogen plasma (T=4720 K, P=1 atm, ρ_e=135, ρ_N=8.1).

Term from Eqn. (13)	s^{-1}	Description
$k_{v=13}^{pred}$	2.6×10^{8}	Predissociation
$\sum A_{13v''}$	2.0×10^{6}	Radiation
$n_M\left(k_{VT}^{13\to14}+k_{VT}^{13\to12}\right)$	6×10^{6}	Vibrational-translational excitation
$n_e k_{ion}^{e}$	negligible	Electron impact ionization
$n_e k_{B,13\to X}^{e}$	3.7×10^{4}	Electron impact excitation to X state
$n_e k_{B,13\to A}^{e}$	3.7×10^{5}	Electron impact excitation to A state
$n_e k_{B,13\to W}^{e}$	3.7×10^{6}	Electron impact excitation to W state
$n_e k_{B,13\to B'}^{e}$	3.8×10^{4}	Electron impact excitation to B' state
$n_e k_{B,13\to C}^{e}$	60	Electron impact excitation to C state

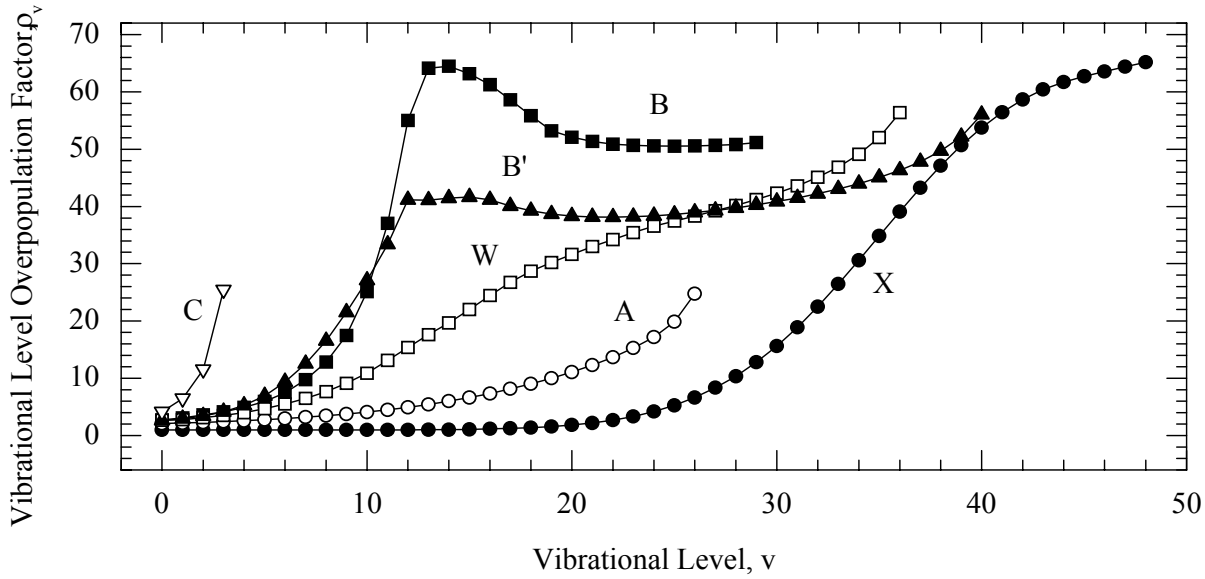


Figure 34. Vibrational overpopulation factors of the X, A, B, W, B′ and C states of N_2. Same conditions as curve (a) of Figure 33

6. Conclusions

Significant advances in Fourier-transform spectroscopy (FTS) and computational chemistry during the past decades have resulted in a wealth of accurate spectroscopic information for most radiative transitions of importance in air plasmas. Thanks to these results, equilibrium radiation codes are now well in hand and can predict equilibrium radiation with a typical accuracy of the order of 20%. However, it should be emphasized that most FTS measurements have been performed in relatively cold sources in which only the low-lying rotational levels are observed (typically up to J=30). Currently our radiation models rely on extrapolations of these FTS results to predict the high rotational levels (often up to J=100) commonly observed in plasmas. Plasma radiation modeling could clearly benefit from FTS measurements in hot sources.

Because the characterization of re-entry flow radiation by onboard detectors can only be conveniently performed using optical emission spectroscopy, it is clear that accurate CR models are needed to infer species concentrations and temperatures from emission measurements. Collisional-radiative models have recently emerged that can predict certain nonequilibrium plasma conditions reasonably well. In this lecture, we showed how a nitrogen CR model can be used to understand and predict the nonequilibrium radiation emitted by a recombining nitrogen plasma at atmospheric pressure. One important result was that the nonequilibrium emission from the N_2 B state can be used to measure the concentration of ground state atomic nitrogen, hence the dissociation fraction of nitrogen in the flow-field. Previously, the only methods to measure ground state nitrogen concentration were VUV absorption and two-photon LIF, which are considerably more difficult to implement than the presently proposed technique.

The reader should be aware that considerable uncertainties remain on many of the state-specific reaction rates. Accurate cross-sections are needed, in particular for state-specific electron and heavy-particle impact dissociation and excitation rate coefficients. At low pressure, it is also important to take into account possible departures from a Maxwellian distribution for the free electrons [82]. Finally, detailed measurements in nonequilibrium flows are required to test and validate the nonequilibrium models.

7. Acknowledgments

The author is pleased to acknowledge contributions to this work by Richard Gessman, Benoit Hilbert, Laurent Pierrot, Sophie Chauveau, Dan Kelley, Denis Packan, Lan Yu, and Charles Kruger. Financial support from the US Air Force Office of Scientific Research, NASA Ames Research Center, and the European Space Agency is gratefully acknowledged.

8. References

[1] G. P. Menees, "Thermal-protection requirements for near-Earth aeroassisted orbital-transfer vehicle missions," *AIAA 83-1513*, 18th AIAA Thermophysics Conference, Montreal, 1983.

[2] L. C. Hartung, R. A. Mitcheltree, and P. A. Gnoffo, "Coupled Radiation Effects in Thermochemical Nonequilibrium Shock-Capturing Flowfield Calculations," *J. Thermophys. Heat Transfer*, vol. 8, pp. 244-250, 1994.

[3] W. D. Henline and M. E. Tauber, "Trajectory-based heating analysis for the ESA/Rosetta Earth return vehicle," *AIAA 93-0269*, 31st Aerospace Sciences Meeting & Exhibit, Reno, NV, 1993.

[4] D. A. Levin, G. V. Candler, R. J. Collins, P. Erdman, E. Zipf, P. Espy, and C. Howlett, "Comparison of Theory with Experiment for the Bow Shock Ultraviolet Rocket Flight Experiment," *J. Thermophys. Heat Transfer*, vol. 7, pp. 30-36, 1993.

[5] G. V. Candler, D. A. Levin, R. J. Collins, P. W. Erdman, E. Zipf, P. Espy, and C. Howlett, "Comparison of theory with plume radiance measurements from the Bow Shock Ultraviolet 2 rocket flight," *J. Thermophys. Heat Transfer*, vol. 7, pp. 709, 1993.

[6] I. Boyd, W. Phillips, and D. Levin, "Prediction of ultra-violet radiation in nonequilibrium hypersonic bow-shock waves," *J. Thermophys. Heat Transfer*, vol. 12, pp. 38, 1998.

[7] P. Jenniskens, M. de Lignie, H. Betlem, J. Borovicka, C. O. Laux, D. Packan, and C. H. Kruger, "Preparing for the 1998/1999 Leonid Storms," in *Laboratory Astrophysics and Space Research*, H. K. P. Ehrenfreund, Ed.: Kluwer Academic Publishers, 1999, pp. 425-455.

[8] C. Park, *Nonequilibrium Hypersonic Aerothermodynamics*. New York: Wiley, 1989.

[9] R. A. Allen, P. H. Rose, and J. C. Camm, "Nonequilibrium and equilibrium radiation at super-satellite re-entry velocities," AVCO Research Laboratory, Everett, MA RR-156, 1962.

[10] W. A. Page and J. O. Arnold, "Shock-Layer Radiation of Blunt Bodies at Reentry Velocities," NASA-Ames Research Center, Moffett Field, CA, Technical Report R-193, April 1964.

[11] R. M. Nerem and G. H. Stickford, "Shock-Tube Studies of Equilibrium Air Radiation," *AIAA Journal*, vol. 3, pp. 1011-1018, 1965.

[12] D. L. Cauchon, "Radiative Heating Results from the Fire 2 Flight Experiment at a Reentry Velocity of 11.4 Kilometers per Second," NASA, TM X-1402, 1967.

[13] R. U. Krey and J. C. Morris, "Experimental Total and Total Line Radiation of Nitrogen, Oxygen, and Argon Plasmas," *Phys. Fluids*, vol. 13, pp. 1483-1487, 1970.

[14] D. M. Curry and E. W. Stephens, "Apollo Ablator Thermal Performance at Super-Orbital Entry Velocities," NASA, TN D-5969, 1970.

[15] D. B. Lee and W. D. Goodrich, "The Aerothermodynamic Environment of the Apollo Command Module during Super-Orbital Entry," NASA, TN D-6792, 1972.

[16] P. W. Schreiber, A. M. Hunter, and K. R. Benedetto, "Electrical Conductivity and Total Emission Coefficient of Air Plasma," *AIAA J.*, vol. 11, pp. 815-821, 1973.

[17] A. Seiff, D. E. Reese, S. C. Sommer, D. B. Kirk, E. E. Whiting, and H. B. Niemann, "PAET, an Entry Probe Experiment in the Earth's Atmosphere," *Icarus*, vol. 18, pp. 525-563, 1973.

[18] S. P. Sharma, W. D. Gillespie, and S. A. Meyer, "Shock Front Radiation Measurements in Air," *AIAA 91-0573*, 1991.

[19] P. W. Erdman, E. C. Zipf, P. Espy, L. C. Howlett, D. A. Levin, R. J. Collins, and G. V. Candler, "Measurements of Ultraviolet-Radiation from a 5-km/s Bow Shock," *J. Thermophys. Heat Transfer*, vol. 8, pp. 441-446, 1994.

[20] D. S. Babikian, N. K. J. M. Gopaul, and C. Park, "Measurement and Analysis of Nitric-Oxide Radiation in an Arcjet Flow," *J. Thermophys. Heat Transfer*, vol. 8, pp. 737-743, 1994.

[21] M. A. Rob, L. H. Mack, and C. D. Scott, "Characterization of Plenum Spectra in an Arcjet Wind-Tunnel," *J. Thermophys. Heat Transfer*, vol. 11, pp. 339-345, 1997.

[22] C. S. Park, M. E. Newfield, D. G. Fletcher, T. Gokçen, and S. P. Sharma, "Spectroscopic Emission Measurements within the Blunt-Body Shock Layer in an Arcjet Flow," *J. Thermophys. Heat Transfer*, vol. 12, pp. 190-197, 1998.

[23] T. Gokçen, C. S. Park, M. E. Newfield, and D. G. Fletcher, "Computational Simulation of Emission Spectra from Shock-Layer Flows in an Arcjet Facility," *J. Thermophys. Heat Trasnfer*, vol. 12, pp. 180-189, 1998.

[24] B. Kivel and K. Bailey, "Tables of radiation from high temperature air," AVCO Research Lab., Research Report 21, Dec. 1957.

[25] R. E. Meyerott, J. Sokoloff, and R. W. Nicholls, "Absoprtion coefficients of air," Geophysics Research Directorate TR-60-277, July 1960.

[26] M. Nardone, R. G. Breene, S. S. Zeldin, and T. R. Riethof, "Radiance of species in high temperature air," General Electric Space Sciences Laboratory, Philadelphia, PA, Report R63SD3, 1963.

[27] R. A. Allen, "Air radiation tables," NASA, Scientific and Technical Information Division, Washington, DC 20546 NASA CR-557, August 1966.

[28] E. E. Whiting, J. O. Arnold, and G. C. Lyle, "A Computer Program for a Line-by-line Calculation of Spectra from Diatomic Molecules and Atoms Assuming a Voigt Line Profile," NASA-Ames Research Center, Moffett Field, CA TN D-5088, 1969.

[29] J. O. Arnold, E. E. Whiting, and G. C. Lyle, "Line by line calculation of spectra from diatomic molecules and atoms assuming a Voigt line profile," *JQSRT*, vol. 9, pp. 775-798, 1969.

[30] C. O. Laux, S. Moreau, and C. H. Kruger, "Experimental Study and Improved Modeling of High-Temperature Air Radiation," *AIAA 92-2969*, 23rd AIAA Plasmadynamics and Lasers Conference, Nashville, TN, 1992.

[31] S. Moreau, C. O. Laux, D. R. Chapman, and R. W. MacCormack, "A more accurate nonequilibrium air radiation code: NEQAIR second generation," *AIAA 92-2968*, 23rd AIAA Plasmadynamics and Lasers Conference, Nashville, TN, 1992.

[32] C. O. Laux, "Optical Diagnostics and Radiative Emission of Air Plasmas," in *Mechanical Engineering*. Stanford, CA: Stanford University, 1993, pp. 232.

[33] C. O. Laux, R. J. Gessman, and C. H. Kruger, "Modeling the UV and VUV Radiative Emission of High-Temperature Air," *AIAA 93-2802*, 28th AIAA Thermophysics Conference, Orlando, FL, 1993.

[34] C. O. Laux, R. J. Gessman, B. Hilbert, and C. H. Kruger, "Experimental Study and Modeling of Infrared Air Plasma Radiation," *AIAA 95-2124*, 30th AIAA Thermophysics Conference, San Diego, CA, 1995.

[35] D. M. Packan, R. J. Gessman, L. Pierrot, C. O. Laux, and C. H. Kruger, "Measurement and Modeling of OH, NO, and CO_2 Infrared Radiation in a Low Temperature Air Plasma," *AIAA 99-3605*, 30th AIAA Plasmadynamics and Lasers Conference, Norfolk, VA, 1999.

[36] S. M. Chauveau, "Constitution d'une Base de Données Spectroscopiques Relatives à un Plasma d'Air," in *Laboratoire EM2C*. Chatenay-Malabry: Ecole Centrale Paris, 2001.

[37] C. Park, "Calculation of Nonequilibrium Radiation in the Flight Regimes of Aeroassisted Orbital Transfer Vehicles," in *Thermal Design of Aeroassisted Orbital Transfer Vehicles*, vol. 96, *Progress in Aeronautics and Astronautics*, H. F. Nelson, Ed.: AIAA, 1985, pp. 395-418.

[38] C. Park, "Nonequilibrium Air Radiation (NEQAIR) Program: User's Manual," NASA-Ames Research Center, Moffett Field, CA, Technical Memorandum TM86707, 1985.

[39] L. C. Hartung, "Development of a Nonequilibrium Radiative Heating Prediction Method for Coupled Flowfield Solutions," *J. Thermophys. Heat Trasfer*, vol. 6, pp. 618-625, 1992.

[40] E. E. Whiting, C. Park, L. Yan, J. O. Arnold, and J. A. Paterson, "NEQAIR96, Nonequilibrium and Equilibrium Radiative Transport and Spectra Program: User's Manual.," NASA, Reference Publication 1389, December 1996.

[41] W. Demtröder, *Laser Spectroscopy*, 3rd corrected printing ed. Berlin: Springer-Verlag, 1988.

[42] P. A. M. Dirac, "The Quantum Theory of the Emission and Absorption of Radiation," *Proc. Royal Soc. London A*, vol. 114, pp. 243-265, 1927.

[43] W. L. Wiese, J. R. Fuhr, and T. M. Deters, *Atomic Transition Probabilities of Carbon, Nitrogen, and Oxygen. A Critical Data Compilation.*, vol. Monograph 7, 1996.

[44] W. C. Martin, J. R. Fuhr, D. E. Kelleher, A. Musgrove, J. Sugar, W. L. Wiese, P. J. Mohr, and K. Olsen, "NIST Atomic Spectra Database Ver. 2.0," Online: http://physics.nist.gov/asd, 1999.

[45] J. M. Brown, J. T. Hougen, K.-P. Huber, J. W. C. Johns, I. Kopp, H. Lefebvre-Brion, A. J. Merer, D. A. Ramsay, J. Rostas, and R. N. Zare, "The labeling of parity doublet levels in linear molecules," *J. Molec. Spectrosc.*, vol. 55, pp. 500-503, 1975.

[46] F. R. Gilmore, "Potential Energy Curves for N_2, NO, O_2, and Corresponding Ions," RAND Corporation, Memorandum R-4034-PR, June 1964.

[47] G. Herzberg, *Molecular Spectra and Molecular Structure I. Spectra of Diatomic Molecules*, vol. I., Second ed. New York, NY: Van Nostrand Reinhold, 1950.

[48] P. F. Bernath, *Spectra of Atoms and Molecules*. New York: Oxford University Press, 1995.

[49] J. I. Steinfeld, *Molecules and Radiation*, Second Edition ed. Cambridge, MA: MIT Press, 1985.

[50] E. E. Whiting, "Rotational line intensity factors for dipole transitions in diatomic molecules," in *Physics Department*. Toronto, Ontario: York University, 1972.

[51] F. Roux, F. Michaud, and J. Vergès, "High-resolution Fourier spectrometry of $^{14}N_2$ infrared emission spectrum: Extensive analysis of the $B^3\Pi_g \rightarrow A^3\Sigma_u^+$ system," *J. Molec. Spectrosc.*, vol. 97, pp. 253-265, 1983.

[52] F. Roux and F. Michaud, "Investigation of the rovibrational levels of the $B^3\Pi_g$ state of $^{14}N_2$ molecule above the dissociation limit $N(^4S) + N(^4S)$ by Fourier transform spectrometry," *Can. J. Phys.*, vol. 68, pp. 1257-1261, 1990.

[53] C. O. Laux and C. H. Kruger, "Arrays of radiative transition probabilities for the N_2 first and second positive, NO beta and gamma, N_2^+ first negative, and O_2 Schumann-Runge band systems," *JQSRT*, vol. 48, pp. 9-24, 1992.

[54] I. Kovacs, *Rotational Structure in the Spectra of Diatomic Molecules*. New York: American Elsevier Publishing Company, Inc., 1969.

[55] J. T. Hougen, "The Calculation of Rotational Energy Levels and Rotational Line Intensities in Diatomic Molecules," NBS, Monograph 115, 1970.

[56] E. E. Whiting, "Computer program for determining rotational line intensity factors for diatomic molecules," NASA Ames Research Center, Moffett Field, CA, Technical Note TN D-7268, Sept. 1973.

[57] R. N. Zare, *Angular Momentum*: John Wiley & Sons, 1988.

[58] J. O. Hornkohl, "Diatomic parity and exchange symmetry," *in preparation*, 1999.

[59] C. O. Laux, R. J. Gessman, and C. H. Kruger, "Mechanisms of Ionizational Nonequilibrium in Air and Nitrogen Plasmas," *AIAA 95-1989*, 26th AIAA Plasmadynamics and Lasers Conference, San Diego, CA, 1995.

[60] R. J. Gessman, C. O. Laux, and C. H. Kruger, "Experimental study of kinetic mechanisms of recombining atmospheric pressure air plasmas," *AIAA 97-2364*, 28th AIAA Plasmadynamics and Lasers Conference, Atlanta, GA, 1997.

[61] T. G. Owano, M. H. Gordon, and C. H. Kruger, "Measurements of the radiation source strength in argon at temperatures between 5000 and 10000 K," *Physics of Fluids B (Plasma Physics)*, vol. 2, pp. 3184-90, 1990.

[62] R.J. Kee, F.M. Rupley, and J.A. Miller, "Chemkin-II: A Fortran Chemical Kinetics Package for the Analysis of Gas Phase Chemical Kinetics," Sandia National Lab., Livermore, CA, SAND89-8009, 1989.

[63] M. G. Dunn and S.-W. Kang, "Theoretical and Experimental Studies of Reentry Plasmas," NASA CR-2232, April 1973.

[64] C. Park, "Review of Chemical-Kinetic Problems of Future NASA Missions, I: Earth Entries," *Journal of Thermophysics and Heat Transfer*, vol. 7, pp. 385-398, 1993.

[65] R. N. Gupta, J. M. Yos, R. A. Thompson, and K.-P. Lee, "A Review of Reaction Rates and Thermodynamic and Transport Properties for an 11-Species Air Model for Chemical and Thermal Nonequilibrium Calculations to 30,000 K," NASA RP-1232, August 1990.

[66] A. M. Gomès, J. Bacri, J. P. Sarrette, and J. Salon, "Measurement of Heavy Particle Temperature in a RF Air Discharge at Atmospheric Pressure from the Numerical Simulation of the NOγ System," *Journal of Analytical Atomic Spectroscopy*, vol. 7, pp. 1103-1109, 1992.

[67] G. E. Gadd, D. L. Huestis, and T. G. Slanger, "Rotational Level-Dependent Radiative Lifetimes and Branching Ratios in NO($B^2\Pi$) (v=7, Ω=1/2,3/2)," *Journal of Chemical Physics*, vol. 95, pp. 3944, 1991.

[68] F. Michaud, F. Roux, S. P. Davis, and A.-D. Nguyen, "High-resolution Fourier spectrometry of N_2^+," *Appl. Optics*, vol. 35, pp. 2867-2873, 1996.

[69] F. Michaud, F. Roux, S. P. Davis, A.-D. Nguyen, and C. O. Laux, "High resolution Fourier spectrometry of the $^{14}N_2^+$ ion," *J. Molec. Spectrosc.*, vol. 203, pp. 1-8, 2000.

[70] C. O. Laux, R. J. Gessman, C. H. Kruger, F. Roux, F. Michaud, and S. P. Davis, "Rotational Temperature Measurements in Air and Nitrogen Plasmas Using the First Negative System of N_2^+," *JQSRT*, vol. 68, pp. 473-482, 2001.

[71] D. Stahel, M. Leoni, and K. Dressler, "Nonadiabatic representations of the $^1\Sigma_u^+$ and $^1\Pi_u$ states of the N_2 molecule," *J. Chem. Phys.*, vol. 79, pp. 2541-2558, 1983.

[72] J. Bacri and A. Medani, "Electron Diatomic Molecule Weighted Total Cross Section Calculation. III. Main Inelastic Processes for N_2 and N_2^+," *Physica C*, vol. 112, pp. 101-118, 1982.

[73] J. P. Sarrette, A. M. Gomes, J. Bacri, C. O. Laux, and C. H. Kruger, "Collisional-Radiative Modelling of Quasi-Thermal Air Plasmas with Electronic Temperatures between 2000 and 13000 K. II. $2000 \leq \Theta_e \leq 4000$ K," *JQSRT*, vol. 53, pp. 143-152, 1995.

[74] J. P. Sarrette, A. M. Gomès, J. Bacri, C. O. Laux, and C. H. Kruger, "Collisional-Radiative Modeling of Quasi-Thermal Air Plasmas with Electronic Temperatures between 2000 and 13,000 K-I. $\Theta_e > 4000$ K," *JQSRT*, vol. 53, pp. 125-141, 1995.

[75] P. Teulet, S. J.-P., and A.-M. Gomès, "Collisional-radiative modelling of one- and two-temperature air and air-sodium plasmas at atmospheric pressure with temperatures of 2000-12 000 K," *JQSRT*, vol. 70, pp. 159-187, 2001.

[76] M. Cacciatore, M. Capitelli, and C. Gorse, "Nonequilibrium Dissociation and Ionization of Nitrogen in Electrical Discharges: the Role of Electronic Collisions from Vibrationally Excited Molecules," *Chemical Physics*, vol. 66, pp. 141-151, 1982.

[77] J. Loureiro and C. M. Ferreira, "Electron Excitation Rates and Transport Parameters in Direct-current N2 Discharges," *Journal of Physics D*, vol. 22, pp. 67-75, 1989.

[78] L. Pierrot, C. O. Laux, and C. H. Kruger, "Vibrationally-Specific Collisional-Radiative Model for Nonequilibrium Nitrogen Plasmas," *AIAA 98-2664*, 29th AIAA Plasmadynamics and Lasers Conference, Albuquerque, NM, 1998.

[79] L. Pierrot, L. Yu, R. J. Gessman, C. O. Laux, and C. H. Kruger, "Collisional-radiative modeling of nonequilibrium effects in nitrogen plasmas," *AIAA 99-3478*, 30th AIAA Plasmadynamics and Lasers Conference, Norfolk, VA, 1999.

[80] L. Pierrot, "Chemical Kinerics and Vibrationally Specific Collisional-Radiative Models for Nonequilibrium Nitrogen Plasmas," Stanford University, ESA Report July 1999.

[81] S. M. Chauveau, C. O. Laux, J. D. Kelley, and C. H. Kruger, "Vibrationally Specific Collisional-Radiative Model for Nonequilibrium Air Plasmas," *AIAA 2002-2229*, 33rd AIAA Plasmadynamics and Lasers Conference, Maui, HW, 2002.

[82] G. Colonna, M. Capitelli, and D. Giordano, "State to State Electron and Vibrational Kinetics in Supersonic Nozzle Expansion: an Improved Model," *AIAA 2002-2163*, 33rd AIAA Plasmadynamics and Lasers Conference, Maui, HW, 2002.

[83] J. Bacri and A. Medani, "Electron Diatomic Molecule Weighted Total Cross Section Calculation. I. Principles for Calculation," *Physica C*, vol. 101, pp. 399-409, 1980.

[84] W. Hwang, Y.-K. Kim, and M. E. Rudd, "New Model for Electron-Impact Ionization Cross Sections of Molecules," *J. Chem. Phys.*, vol. 104, pp. 2956-2966, 1996.

[85] T. Majeed and D. J. Strickland, "New Survey of Electron Impact Cross Sections for Photoelectron and Auroral Electron Energy Loss Calculations," *J. Phys. Chem. Ref. Data*, vol. 26, pp. 335-349, 1997.

[86] J. R. Peterson, A. Le Padellec, H. Danared, G. H. Dunn, M. Larrson, A. Larson, R. Peverall, C. S. R. Stromhlom, M. af Ugglas, and W. J. van der Zande, "Dissociative Recombination and Excitation of N_2^+: Cross Sections and Product Branching Ratios," *J. Chem. Phys.*, vol. 108, pp. 1978-1988, 1998.

[87] R. F. Stebbings, B. R. Turner, and A. C. H. Smith, *Journal of Chemical Physics*, vol. 38, pp. 2277, 1963.

[88] D. C. Cartwright, S. Trajmar, A. Chutjian, and W. Williams, "Electron Impact Excitation of the Electronic States of N_2. II. Integral Cross Sections at Incident Energies from 10 to 50 eV," *Physical Review A*, vol. 16, pp. 1041-1051, 1977.

[89] M. J. Seaton, "The Theory of Excitation and Ionization by Electron Impact," in *Atomic and Molecular Processes*, vol. 13, D. R. Bates, Ed.: Academic Press, 1962, pp. 375-420.

[90] Y. K. Kazansky and I. S. Yelets, "The Semiclassical Approximation in the Local Theory of Resonance Inelastic Interaction of Slow Electrons with Molecules," *J. Phys. B*, vol. 17, pp. 4767-4783, 1984.

[91] H. Geisen, D. Neuschäfer, and C. Ottinger, "State-specific Predissociation of $N_2(B^3\Pi_g)$ Measured by Laser-induced Fluorescence on Molecular Beam," *Journal of Chemical Physics*, vol. 92, pp. 104-115, 1990.

[92] J. Bacri and A. Medani, "Electron Diatomic Molecule Weighted Total Cross Section Calculation. II. Application to the Nitrogen Molecule," *Physica C*, vol. 101, pp. 410-419, 1980.